

# Parallel Projection—A New Return Mapping Algorithm for Finite Element Modeling of Shape Memory Alloys

Ziliang Kang<sup>a</sup>, Daniel A. Tortorelli<sup>b,c</sup>, Kai A. James<sup>a</sup>

<sup>a</sup>*Aerospace Engineering, University of Illinois at Urbana-Champaign, Urbana, IL 61801, USA*

<sup>b</sup>*Mechanical Science and Engineering, University of Illinois at Urbana-Champaign, Urbana, IL 61801, USA*

<sup>c</sup>*Lawrence Livermore National Laboratory, Livermore, CA 94550, USA*

---

## Abstract

We present a novel method for finite element analysis of inelastic structures containing Shape Memory Alloys (SMAs). Phenomenological constitutive models for SMAs lead to material nonlinearities, that require substantial computational effort to resolve. Finite element analysis methods, which rely on Gauss quadrature integration schemes, must solve two sets of coupled differential equations: one at the global level and the other at the local, i.e. Gauss point level. In contrast to the conventional return mapping algorithm, which solves these two sets of coupled differential equations separately using a nested Newton procedure, we propose a scheme to solve the local and global differential equations simultaneously. In the process we also derive closed-form expressions used to update the internal state variables, and unify the popular closest-point and cutting plane methods with our formulas. Numerical testing indicates that our method allows for larger thermomechanical loading steps and provides increased computational efficiency, over the standard return mapping algorithm.

*Keywords:* shape-memory alloys, computational inelasticity, finite element analysis, return mapping algorithm, parallel projection algorithm

---

## 1. Introduction

In the past three decades, shape memory alloys (SMAs) have become one of the most widely used active materials. The actuating features of SMAs come from the Two-Way Shape Memory Effect (TWSME) and pseudoelasticity (superelasticity). These terms refer to recoverable deformations due to a temperature cycle and a mechanical loading cycle, respectively. These properties, as well as the characteristics of high energy density, medium-to-high actuating frequency, and favourable mechanical properties (strength, stiffness, etc.), have made SMAs a frequent choice in a variety of applications [1].

Given these advantages, computational modelling of SMAs is an important topic of investigation. Specifically, constitutive modeling and finite element analysis of polycrystalline SMAs are of critical importance, since many polycrystalline SMAs tend to exhibit stable TWSMEs and superelasticity [2]. However, the complex constitutive relationship of these multifunctional materials substantially increases the difficulty of the modeling task. Various thermomechanical constitutive models for SMAs have been developed and these models can generally be categorized into two groups—micromechanical models and phenomenological models. While micromechanical models focus more on describing the microscopic behaviors of different variants and lattice structures within the SMA family, phenomenological models concentrate on macroscopic constitutive behaviors.

Sun and Hwang produced pioneering work on constitutive relationships based on micromechanical models [3, 4]. Further study on the micromechanical dynamics of phase boundary motion was then conducted by Bhattacharya [5, 6]. In the past decade, researchers in this area have further investigated the lattice structure of SMAs, and have sought to develop models that can accurately capture the phenomena of twinning, detwinning, and single crystallization [7, 8]. Micromechanics models are computationally intense, and produce a level of details that may not be necessary for all applications. This gives rise to phenomenological models, whose main challenge is to accurately model hardening during phase transformation. The exponential hardening rule is the first proposed model for NiTi SMAs[9], followed by the cosine model [10, 11], the quadratic function model [12, 13, 14] and the smooth transformation model [15]. These phenomenological models formed the basis of improved constitutive models considering plasticity [16, 17], creep [18, 19, 20], tension-compression asymmetry [21, 22] and large deformation [23]. Efforts in this area are also directed toward introducing different representations for thermodynamic potentials, which contain internal state variables that represent the transformation state of SMAs. As a result, finite element analysis of SMAs has become more computationally efficient, with fewer tuned parameters. Indeed, experimental data are replicated with these thermodynamic constitutive relations. Formulations using potential energy wells, Helmholtz free energy potential, Gibbs free energy and phase diagrams have been reported [24, 25, 26, 27, 28]. Though these phenomenological models are not as accurate as the micromechanical models at the lattice (molecular) scale, their simplicity makes them computationally efficient and easily implemented in finite element analysis of macro-scale structures.

For both micromechanical and phenomenological models, finite element analysis require iterative techniques to evaluate the dynamic thermal energy state of the material [29] at each time step within the simulation. Two sets of coupled differential equations (DEs) need to be solved concurrently. One set contains the global partial differential equations (PDEs) based on the momentum balance, and the other set contains the local ordinary differential equations (ODEs), which are based on the evolution relation [30]. Extensive applied mathematics research has been focused on solving these large coupled systems of DEs efficiently. The return mapping algorithm is the most wide-adopted approach [31]. This method is a sequential/nested approach. In each iteration one first updates the internal/constitutive state variables for the given state of strain by solving local constitutive DEs at each Gauss point. Then the displacement is updated by solving the linear system derived from the global equilibrium PDEs.

We propose an improved return mapping algorithm, in which we simultaneously solve the local and global governing DEs. While similar procedures have been implemented for plasticity [32], researchers have yet to apply these tools to SMAs due to the complicated schemes required for updating the internal state variables. We refer to our approach as the *parallel projection* algorithm. The algorithm is able to provide identical results, when compared with the classical return mapping algorithm, with measurable bearing of larger themomechanical loading steps and computational savings. In the sections that follow, we explain the implementation and mathematical rationale behind the algorithm, and demonstrate the algorithm via a series of example problems containing one- and three dimensional domains.

## 2. Methodology

### 2.1. Phenomenological Constitutive Relationship of SMAs

The unique properties (TWSME and superelasticity) of SMAs are triggered by a non-diffusional phase transformation, which is caused by latent heat exchange between two stable phases. These two phases, martensite (M) and austenite (A), are each characterized by their distinctive molecular

lattice structures. In this paper, we use the phenomenological constitutive models derived by Boyd and Lagoudas [12] and later described by Lagoudas in 2008 [14]. This model uses the Gibbs-free energy,

$$G = u - \frac{1}{\rho} \boldsymbol{\sigma} : \boldsymbol{\varepsilon} - sT \quad (1)$$

to build the constitutive relationship. Here,  $\boldsymbol{\varepsilon}$  refer to the total strain tensor,  $\boldsymbol{\sigma}$  is the stress tensor,  $T$  is the temperature,  $\rho$  is the density,  $u$  is the specific internal energy and  $s$  is the specific entropy which define the energy state of the thermodynamic system. The operator “:” refers to double dot product of tensors. The choice of Gibbs free energy makes it easier to represent the constitutive model in the global momentum balance relationship used in the finite element analysis. We assume that the energy function  $G$  depends on the martensite volume fraction  $\xi$ , the stress  $\boldsymbol{\sigma}$ , the temperature  $T$ , and the transformation strain  $\boldsymbol{\varepsilon}^t$ . It is further assumed to be expressed as the sum of bulk  $G_b$  and mixing  $G_m$  energies such that

$$G = G_b + G_m \quad (2)$$

where

$$G_b(\xi, \boldsymbol{\sigma}, T) = -\frac{1}{2\rho} \boldsymbol{\sigma} : \boldsymbol{S} : \boldsymbol{\sigma} - \frac{1}{\rho} \boldsymbol{\sigma} : \boldsymbol{\alpha} (T - T_0) + c \left[ (T - T_0) - T \ln \frac{T}{T_0} \right] - s_0 T + u_0 \quad (3)$$

and

$$G_m(\xi, \boldsymbol{\sigma}, T, \boldsymbol{\varepsilon}^t) = -\frac{1}{\rho} \boldsymbol{\sigma} : \boldsymbol{\varepsilon}^t + \frac{1}{\rho} f(\xi) \quad (4)$$

In the above  $f$  is the transformation hardening function defining the specific energy due to mixing and can be obtained from experiments,  $T_0$  refers to reference temperature for thermal expansion,  $\boldsymbol{S}$  is the compliance tensor and  $\boldsymbol{\alpha}$  is the thermal expansion tensor. For isotropic SMAs, the Young’s modulus  $E$  is the only variant in the evolution of the compliance tensor  $\boldsymbol{S}$ . As such, we express  $\boldsymbol{S}$  (in Voight notation) via the compliance modulus  $S = 1/E$  and the Poisson’s ratio  $\nu$  as

$$\boldsymbol{S} = S \boldsymbol{\mathfrak{e}} \quad (5)$$

$$\boldsymbol{\mathfrak{e}} = \begin{bmatrix} 1 & -\nu & -\nu & 0 & 0 & 0 \\ -\nu & 1 & -\nu & 0 & 0 & 0 \\ -\nu & -\nu & 1 & 0 & 0 & 0 \\ 0 & 0 & 0 & 2(1+\nu) & 0 & 0 \\ 0 & 0 & 0 & 0 & 2(1+\nu) & 0 \\ 0 & 0 & 0 & 0 & 0 & 2(1+\nu) \end{bmatrix}$$

Consistent with our isotropic assumption, the thermal expansion tensor  $\boldsymbol{\alpha}$  is given by

$$\boldsymbol{\alpha} = \alpha \cdot \text{diag} ( 1, 1, 1, 0, 0, 0 ) \quad (6)$$

where  $\alpha$  is the thermal expansion coefficient.

The symbols  $c$ ,  $s_0$  and  $u_0$  in Equation 3 represent the effective specific heat, effective specific entropy and effective specific internal energy. The values of the above physical quantities are expressed as a volume average of their values in their martensite (M) and austenite (A) phases, i.e.

$$\begin{aligned} S &= S^A + \xi(S^M - S^A) = S^A + \xi \Delta S \\ \alpha &= \alpha^A = \alpha^M \\ c &= c^A = c^M \\ s_0 &= s_0^A + \xi(s_0^M - s_0^A) = s_0^A + \xi \Delta s_0 \\ u_0 &= u_0^A + \xi(u_0^M - u_0^A) = u_0^A + \xi \Delta u_0 \end{aligned} \quad (7)$$

Note that  $\alpha$  and  $c$  are assumed to be constant

The total strain tensor of SMAs  $\boldsymbol{\varepsilon}$  can be derived by substituting Equation 1 and 2 into the second law of thermodynamics.

$$\frac{1}{\rho} \boldsymbol{\sigma} : \dot{\boldsymbol{\varepsilon}} - (\dot{u} + \dot{s}T) \geq 0 \quad (8)$$

Applying the Coleman-Noll approach [30], we find that the total strain is composed of three parts, i.e.

$$\boldsymbol{\varepsilon} = \boldsymbol{\varepsilon}^e + \boldsymbol{\varepsilon}^{th} + \boldsymbol{\varepsilon}^t \quad (9)$$

In the above we have the usual elastic strain  $\boldsymbol{\varepsilon}^e = \mathbf{S} : \boldsymbol{\sigma}$  and pure thermal expansion strain  $\boldsymbol{\varepsilon}^{th} = \boldsymbol{\alpha}(T - T_0)$ , and the transformation strain  $\boldsymbol{\varepsilon}^t$ , which is defined via a phenomenological model. We can invert the relation to obtain the familiar looking result

$$\begin{aligned} \boldsymbol{\sigma} &= \mathbf{S}^{-1} : (\boldsymbol{\varepsilon} - \boldsymbol{\varepsilon}^{th} - \boldsymbol{\varepsilon}^t) \\ &= \mathbf{S}^{-1} : (\boldsymbol{\varepsilon} - \boldsymbol{\alpha}(T - T_0) - \boldsymbol{\varepsilon}^t) \end{aligned} \quad (10)$$

An evolution relation (flow rule) [33] is proposed to build a relationship between the transformation strain  $\boldsymbol{\varepsilon}^t$  and the martensite volume fraction  $\xi$ . Thus we only have three internal variables  $\xi$ ,  $\boldsymbol{\sigma}$  and  $T$  to consider in the phenomenological model. The  $\xi - \boldsymbol{\varepsilon}^t$  relation is governed by the experimentally obtained transformation tensor  $\boldsymbol{\Lambda}$ ; we use the isotropic relationship proposed by Boyd and Lagoudas [12].

$$\begin{aligned} \dot{\boldsymbol{\varepsilon}}^t &= \boldsymbol{\Lambda} \dot{\xi} \\ \boldsymbol{\Lambda} &= \begin{cases} \frac{3}{2} H \frac{\boldsymbol{\sigma}_s}{\sigma_s^{eff}} & \dot{\xi} > 0 \\ H \frac{\boldsymbol{\varepsilon}_{t-r}}{\varepsilon_{t-r}^{eff}} & \dot{\xi} < 0 \end{cases} \end{aligned} \quad (11)$$

where  $H$  is the maximum transformation strain of the SMA material. In the forward transformation, i.e. austenite (A) to martensite (M) transformation for which  $\dot{\xi} > 0$ ,  $\boldsymbol{\sigma}_s$  is the deviatoric stress tensor and  $\sigma_s^{eff}$  is its associated effective (von Mises) stress. In the reverse transformation, i.e. martensite (M) to austenite (A) transformation for which  $\dot{\xi} < 0$ ,  $\boldsymbol{\varepsilon}_{t-r}$  is the transformation strain tensor at the reversal point, and  $\varepsilon_{t-r}^{eff}$  is its associated effective strain.

Using the aforementioned thermodynamic relationships, the second law of thermodynamics reduces to the Clausius-Planck inequality [34].

$$\Pi \dot{\xi} \geq 0 \quad (12)$$

where

$$\Pi(\xi, \boldsymbol{\sigma}, T) = \boldsymbol{\sigma} : \boldsymbol{\Lambda} + \frac{1}{2} \boldsymbol{\sigma} : \Delta \mathbf{S} : \boldsymbol{\sigma} + \rho \Delta s_0 T - \rho \Delta u_0 - \frac{\partial f(\xi)}{\partial \xi} \quad (13)$$

and we recall that the thermal expansion coefficient and specific heat do not change with the phase transformation.

Note that the Clausius-Planck inequality must be satisfied for all admissible thermomechanical loading paths  $\dot{\xi}$ . In our study, the loading paths are constrained such that  $\Phi \leq 0$ , where  $\Phi = |\Pi| - Y$  can be viewed as a type of yield function where  $Y$  is a type of yield strength (transformation threshold) determined by the transformation hardening function. When  $\Phi = 0$ , we have two possibilities. If  $\Pi - Y = 0$  then to satisfy Equation 12,  $\dot{\xi} > 0$ , indicating the forward transformation; otherwise if  $-\Pi - Y = 0$  then  $\dot{\xi} < 0$ , indicating the inverse transformation. For all other cases of thermoelastic behaviors, i.e. for  $\Phi < 0$ , we have  $\dot{\xi} = 0$ .

$$\Phi \begin{cases} = \Pi - Y = 0 & \dot{\xi} > 0 \text{ (A} \rightarrow \text{M)} \\ = -\Pi - Y = 0 & \dot{\xi} < 0 \text{ (M} \rightarrow \text{A)} \\ < 0 & \dot{\xi} = 0 \end{cases} \quad (14)$$

We assume the martensite volume fraction  $\xi$  evolves so as to maximize the dissipation of Equation 13, subject to the  $\Phi \leq 0$  constraint. As such, we must satisfy the Kuhn-Tucker conditions

$$\Phi \leq 0, \quad \Phi \dot{\xi} = 0, \quad \dot{\xi} \begin{cases} \geq 0 & \text{if } \Pi - Y = 0 \quad (\text{A} \rightarrow \text{M}) \\ \leq 0 & \text{if } -\Pi - Y = 0 \quad (\text{M} \rightarrow \text{A}) \\ = 0 & \text{if } \Phi < 0 \end{cases} \quad (15)$$

Additionally, during either forward or reverse transformation, i.e.  $\dot{\xi} \neq 0$ , we must satisfy the consistency condition to stay on the "loading surface", i.e. to maintain the  $\Phi = 0$  equality [35]

$$\dot{\Phi} = \frac{\partial \Phi}{\partial \boldsymbol{\sigma}} : \dot{\boldsymbol{\sigma}} + \frac{\partial \Phi}{\partial T} : \dot{T} + \frac{\partial \Phi}{\partial \xi} : \dot{\xi} = 0 \quad (16)$$

To satisfy the Kuhn-Tucker and the consistency conditions, the following inelastic constitutive relationship must hold

$$\begin{aligned} d\boldsymbol{\sigma} &= \boldsymbol{\mathcal{L}} : d\boldsymbol{\varepsilon} + \boldsymbol{\Theta} : dT \\ \boldsymbol{\mathcal{L}} &= \begin{cases} \mathbf{S}^{-1} - \frac{\mathbf{S}^{-1} : \partial_{\boldsymbol{\sigma}} \Phi \otimes \mathbf{S}^{-1} : \partial_{\boldsymbol{\sigma}} \Phi}{\partial_{\boldsymbol{\sigma}} \Phi : \mathbf{S}^{-1} : \partial_{\boldsymbol{\sigma}} \Phi - \partial_{\xi} \Phi} & \dot{\xi} > 0 \\ \mathbf{S}^{-1} - \frac{\mathbf{S}^{-1} : \partial_{\boldsymbol{\sigma}} \Phi \otimes \mathbf{S}^{-1} : \partial_{\boldsymbol{\sigma}} \Phi}{\partial_{\boldsymbol{\sigma}} \Phi : \mathbf{S}^{-1} : \partial_{\boldsymbol{\sigma}} \Phi + \partial_{\xi} \Phi} & \dot{\xi} < 0 \end{cases} \\ \boldsymbol{\Theta} &= \begin{cases} -\boldsymbol{\mathcal{L}} : \boldsymbol{\alpha} - \partial_T \Phi \frac{\mathbf{S}^{-1} : \partial_{\boldsymbol{\sigma}} \Phi}{\partial_{\boldsymbol{\sigma}} \Phi : \mathbf{S}^{-1} : \partial_{\boldsymbol{\sigma}} \Phi - \partial_{\xi} \Phi} & \dot{\xi} > 0 \\ -\boldsymbol{\mathcal{L}} : \boldsymbol{\alpha} - \partial_T \Phi \frac{\mathbf{S}^{-1} : \partial_{\boldsymbol{\sigma}} \Phi}{\partial_{\boldsymbol{\sigma}} \Phi : \mathbf{S}^{-1} : \partial_{\boldsymbol{\sigma}} \Phi + \partial_{\xi} \Phi} & \dot{\xi} < 0 \end{cases} \end{aligned} \quad (17)$$

where  $\otimes$  refers to the tensor product operator,  $\boldsymbol{\mathcal{L}}$  and  $\boldsymbol{\Theta}$  are the continuum tangent stiffness and tangent thermal moduli.

## 2.2. Finite Element Analysis of SMAs

### 2.3. The Discrete Model

We now describe the combined equilibrium and constitutive DE problem as finding the kinematically admissible displacement  $\mathbf{d}$ , martensite volume fraction  $\xi$ , transformation strain  $\boldsymbol{\varepsilon}^t$  and stress tensor  $\boldsymbol{\sigma}$  such that

$$\begin{aligned} \text{Global Level :} & \quad \text{force equilibrium} & \int_{\Omega} \boldsymbol{\varepsilon}(\delta \mathbf{d}) \boldsymbol{\sigma}(\mathbf{d}, \xi) d\Omega - \int_{\Gamma^P} \delta \mathbf{d} \mathbf{P} d\Gamma^P = 0 \quad \forall \delta \mathbf{d} \\ \text{Local Level :} & \quad \text{KKT - condition} & \Phi \leq 0 \text{ in } \Omega \\ & & \dot{\xi} \Phi = 0 \text{ in } \Omega \\ \text{Consistency} & & \dot{\Phi} = \frac{\partial \Phi}{\partial \boldsymbol{\sigma}} : \dot{\boldsymbol{\sigma}} + \frac{\partial \Phi}{\partial T} : \dot{T} + \frac{\partial \Phi}{\partial \xi} : \dot{\xi} \text{ in } \Omega \\ \text{flow rule} & & \dot{\boldsymbol{\varepsilon}}^t = \boldsymbol{\Lambda} \dot{\xi}, \end{aligned} \quad (18)$$

where the boundary conditions include prescribed displacements  $\mathbf{d}^c$  over  $\Gamma_d$ , prescribed traction  $\mathbf{P}$  over  $\Gamma^P$ , and the temperature  $T$  is prescribed.

From Equation 18, two sets of DEs can be observed — one set of PDEs is applied at the global level, to enforce the equilibrium equation. The other set of ODEs is applied at the local level to enforce the constitutive relationship. Generally, for such complicated systems of differential equations, numerical methods must be used to approximate the response. We discretize the system in the spatial domain via the finite element method and in the time domain via a backward-Euler scheme. Here each pseudo-time step corresponds to a temperature increment or a load increment.

The discretized form of Equation 18 is shown in Equation 19.

$$\begin{aligned}
\text{Global Level : } \mathbf{R}_{n+1} &= \bigwedge_{\text{el}} \left( \sum_G (w \mathbf{B}^T(\mathbf{G}^d) \boldsymbol{\sigma}_{n+1} - \varpi \mathbf{N}(\mathbf{G}^F) \mathbf{p}_{n+1}) \right) = 0 \\
\text{Local Level : } \mathbf{H}_{n+1} &= \left\{ \begin{array}{l} H_\Phi = \Phi(\boldsymbol{\sigma}_{n+1}, T_{n+1}, \xi_{n+1}) \\ \mathbf{H}_{\boldsymbol{\varepsilon}^t} = \boldsymbol{\varepsilon}_n^t + \boldsymbol{\Lambda}(\xi_{n+1} - \xi_n) - \boldsymbol{\varepsilon}_{n+1}^t \\ H_S = S_n + \Delta S(\xi_{n+1} - \xi_n) - S_{n+1} \\ \mathbf{H}_\boldsymbol{\sigma} = \mathbf{S}_{n+1}^{-1} : [\boldsymbol{\varepsilon}_{n+1} - \boldsymbol{\alpha}(T_{n+1} - T_0) - \boldsymbol{\varepsilon}_{n+1}^t] - \boldsymbol{\sigma}_{n+1} \\ \mathbf{H}_{n+1} = \mathbf{S}^{-1} : [\boldsymbol{\varepsilon}_{n+1} - \boldsymbol{\alpha}(T_{n+1} - T_0) - \boldsymbol{\varepsilon}^t] - \boldsymbol{\sigma}_{n+1} = 0 \end{array} \right\} = 0 \quad \begin{array}{l} \dot{\xi} \neq 0 \\ \dot{\xi} = 0 \end{array} \quad (19)
\end{aligned}$$

Here,  $G^d$  ( $G^F$ ) are the number of 2D (1D) Gauss points for the area(line) integrals and  $w$  ( $\varpi$ ) are the corresponding product of differential area (length) and Gauss weights at the Gauss points, respectively.  $\mathbf{N}$  and  $\mathbf{B}$  are shape functions used to interpolate the displacement and strain fields such that, e.g., the total strain tensor can be expressed as  $\boldsymbol{\varepsilon}_{n+1} = \mathbf{B} \mathbf{d}_{n+1}$ .<sup>1</sup>

There are two sets of unknown states in the problem, the global state variable  $\mathbf{u} = (\mathbf{d}^f, \mathbf{F}^c)$ , and the local state variables  $\boldsymbol{\nu} = (\xi, \boldsymbol{\varepsilon}^t, S, \boldsymbol{\sigma})$  for the inelastic case, and  $\boldsymbol{\nu} = \boldsymbol{\sigma}$  for the elastic case. Here,  $f$  refers to the free, i.e. unprescribed displacement degrees of freedom,  $\mathbf{d}^f$ ; and  $c$  represents the unknown reaction forces  $\mathbf{F}^c$  at prescribed, i.e. constrained displacement degrees of freedom.

#### 2.4. The Parallel Projection Algorithm

The aforementioned discrete model yields two sets of DEs equations that are defined in residual form;  $\mathbf{R} = 0$  is the global equilibrium residual, and  $\mathbf{H} = 0$  is the local residual. The two sets of DEs are coupled through the Cauchy stress tensor  $\boldsymbol{\sigma}$  and displacement  $\mathbf{d}$ . This results in a large system of nonlinear equations. For instance, for a two-dimensional (2D) domain with  $N$  nodes and  $G$  Gauss points, the FEM problem contains  $2 \times N$  global equations and up to  $6 \times G$  local equations, all of which must be solved concurrently using the Newton-Raphson method.

To lessen the high computational cost, one's first instinct might be to partition the system, and hence shrink the size of tangent matrix in the Newton-Raphson scheme. In the popular return-mapping algorithm [31], the resulting system is uncoupled as

$$\begin{aligned}
\mathbf{R}(\mathbf{u}, \boldsymbol{\nu}(\mathbf{u})) &= 0 \\
\mathbf{H}(\mathbf{u}, \boldsymbol{\nu}(\mathbf{u})) &= 0
\end{aligned} \quad (20)$$

The uncoupled system is solved separately via a nested Newton-Raphson iteration consisting of two loops,

$$\text{inner loop for } \boldsymbol{\nu}^{(l+1)}: \left\{ \begin{array}{l} \left[ \frac{\partial \mathbf{H}}{\partial \boldsymbol{\nu}}(\mathbf{u}^{(k)}, \boldsymbol{\nu}^{(l)}(\mathbf{u}^{(k)})) \right] \delta \boldsymbol{\nu}^{(l)} = -\mathbf{H}(\mathbf{u}^{(k)}, \boldsymbol{\nu}^{(l)}(\mathbf{u}^{(k)})) \\ \boldsymbol{\nu}^{(l+1)} = \boldsymbol{\nu}^{(l)} + \delta \boldsymbol{\nu}^{(l)}, l = 1, 2, 3, \dots \end{array} \right. \quad (21)$$

$$\text{loop if } \mathbf{H} \neq 0 \quad (22)$$

$$\text{outer loop for } \mathbf{u}^{(k+1)}: \left\{ \begin{array}{l} \left[ \frac{\partial \mathbf{R}}{\partial \mathbf{u}}(\mathbf{u}^{(k)}, \boldsymbol{\nu}^{(l+1)}) - \frac{\partial \mathbf{R}}{\partial \boldsymbol{\nu}} \left( \frac{\partial \mathbf{H}}{\partial \boldsymbol{\nu}} \right)^{-1} \frac{\partial \mathbf{H}}{\partial \mathbf{u}}(\mathbf{u}^{(k)}, \boldsymbol{\nu}^{(l+1)}) \right] \delta \mathbf{u}^{(k)} = -\mathbf{R}(\mathbf{u}, \boldsymbol{\nu}^{(l+1)}) \\ \mathbf{u}^{(k+1)} = \mathbf{u}^{(k)} + \delta \mathbf{u}^{(k)}, k = 1, 2, 3, \dots \end{array} \right.$$

<sup>1</sup>Note that  $H_S$  is the rate form of Equation 7 and could be simplified to  $H_S = S_A + \Delta S \xi_{n+1} - S_{n+1}$ . However, to maintain consistency with [14] and consider experimental data may only provide the value of  $\Delta S$ , we use the rate equation shown.

where  $l$  and  $k$  are the iteration counters of the inner and outer Newton-Raphson loops. The derivative  $d\boldsymbol{\nu}/d\mathbf{u} = -(\partial\mathbf{H}/\partial\boldsymbol{\nu})^{-1}(\partial\mathbf{H}/\partial\mathbf{u})$  in the outer loop is obtained by differentiating the local residual in Equation 20.

$$\frac{\partial\mathbf{H}}{\partial\mathbf{u}}(\mathbf{u}, \boldsymbol{\nu}(\mathbf{u})) + \frac{\partial\mathbf{H}}{\partial\boldsymbol{\nu}}(\mathbf{u}, \boldsymbol{\nu}(\mathbf{u}))\frac{d\boldsymbol{\nu}}{d\mathbf{u}}(\mathbf{u}) = 0 \quad (23)$$

As seen above, the local residual equation  $\mathbf{H} = 0$  in the inner loop is first solved for  $\boldsymbol{\nu}$  via Newton's method for the fixed  $\mathbf{u}$ . After convergence of the inner problem, i.e. after  $|\mathbf{H}| \approx 0$ , we update the displacement  $\mathbf{u}$  by solving the linear system in the outer loop. We repeat the process, i.e. of solving the inner loop residual and updating the displacement until  $|\mathbf{R}| \approx 0$ . Unfortunately, while the return mapping algorithm reduces the size of the tangent matrix in the outer loop, it may require more iterations than simply solving the global system as a single residual. We seek a method that combines the benefits of both approaches.

In response to the aforementioned concern, we introduce the parallel projection algorithm. In this algorithm, we still partition the equation as shown in Equation 20 to diminish the size of the tangent matrix. However, we solve the coupled equations in a cross-iterative Newton-Raphson scheme, which also contains inner and outer computations:

$$\begin{aligned} \text{inner : } & \begin{cases} \left[ \frac{\partial\mathbf{H}}{\partial\boldsymbol{\nu}}(\mathbf{u}^{(k)}, \boldsymbol{\nu}^{(k)}(\mathbf{u}^{(k)})) \right] \delta\boldsymbol{\nu}^{(k)} = -\mathbf{H}(\mathbf{u}^{(k)}, \boldsymbol{\nu}^{(k)}(\mathbf{u}^{(k)})) - \frac{\partial\mathbf{H}}{\partial\mathbf{u}}(\mathbf{u}^{(k)}, \boldsymbol{\nu}^{(k)}(\mathbf{u}^{(k)}))\delta\mathbf{u}^{(k-1)} \\ \boldsymbol{\nu}^{(k+1)} = \boldsymbol{\nu}^{(k)} + \delta\boldsymbol{\nu}^{(k)}, \quad k = 1, 2, 3, \dots \end{cases} \\ \text{outer : } & \begin{cases} \left[ \frac{\partial\mathbf{R}}{\partial\mathbf{u}}(\mathbf{u}^{(k)}, \boldsymbol{\nu}^{(k+1)}) - \frac{\partial\mathbf{R}}{\partial\boldsymbol{\nu}} \left( \frac{\partial\mathbf{H}}{\partial\boldsymbol{\nu}} \right)^{-1} \frac{\partial\mathbf{H}}{\partial\mathbf{u}}(\mathbf{u}^{(k)}, \boldsymbol{\nu}^{(k+1)}) \right] \delta\mathbf{u}^{(k)} \\ = -\mathbf{R}(\mathbf{u}^{(k)}, \boldsymbol{\nu}^{(k)}) + \frac{\partial\mathbf{R}}{\partial\boldsymbol{\nu}} \left( \frac{\partial\mathbf{H}}{\partial\boldsymbol{\nu}} \right)^{-1} \mathbf{H}(\mathbf{u}^{(k)}, \boldsymbol{\nu}^{(k)}) \\ \mathbf{u}^{(k+1)} = \mathbf{u}^{(k)} + \delta\mathbf{u}^{(k)} \end{cases} \end{aligned} \quad (24)$$

Notably, 1) we do not iterate to fully resolve the inner equation, 2) we solve the outer problem in parallel with the inner problem, 3) the coefficient matrices are identical in the return-mapping and parallel projection algorithms. To begin the algorithm, i.e. for  $k = 1$ , we assign  $\delta\mathbf{u}^{(0)} = \mathbf{0}$ . Figure 1 highlights the difference between the return-mapping and parallel projection algorithms.

### 2.5. The Newton-Raphson Scheme for solving the local residual $\mathbf{H}$

In this section, we specifically provides the analytical solution of the updating scheme for the internal state variable  $\boldsymbol{\nu}$ . As seen above in Equation 21 and 24, we need calculate the inverse of the tangent matrix  $\partial\mathbf{H}/\partial\boldsymbol{\nu}$ . Depending on the thermomechanical state of the material, i.e. depending on whether or not  $\xi \approx \xi_{n+1} - \xi_n$  is zero or nonzero we have,

$$\frac{\partial\mathbf{H}_n}{\partial\boldsymbol{\nu}_n} = \begin{cases} \begin{bmatrix} \frac{\partial H_\Phi^n}{\partial \xi_n} & \frac{\partial H_\Phi^n}{\partial \xi_n^t} & \frac{\partial H_\Phi^n}{\partial S_n} & \frac{\partial H_\Phi^n}{\partial \boldsymbol{\sigma}_n} \\ \frac{\partial H_{\boldsymbol{\varepsilon}^t}^n}{\partial \xi_n} & \frac{\partial H_{\boldsymbol{\varepsilon}^t}^n}{\partial \xi_n^t} & \frac{\partial H_{\boldsymbol{\varepsilon}^t}^n}{\partial S_n} & \frac{\partial H_{\boldsymbol{\varepsilon}^t}^n}{\partial \boldsymbol{\sigma}_n} \\ \frac{\partial H_S^n}{\partial \xi_n} & \frac{\partial H_S^n}{\partial \xi_n^t} & \frac{\partial H_S^n}{\partial S_n} & \frac{\partial H_S^n}{\partial \boldsymbol{\sigma}_n} \\ \frac{\partial H_\sigma^n}{\partial \xi_n} & \frac{\partial H_\sigma^n}{\partial \xi_n^t} & \frac{\partial H_\sigma^n}{\partial S_n} & \frac{\partial H_\sigma^n}{\partial \boldsymbol{\sigma}_n} \end{bmatrix} = \begin{bmatrix} \partial_\xi \Phi_n & \mathbf{0}_{1 \times 6} & 0 & \partial_\sigma \Phi_n^T \\ \boldsymbol{\Lambda}_n & -\mathbf{I}_{6 \times 6} & \mathbf{0}_{6 \times 1} & \partial_\sigma \boldsymbol{\Lambda}_n : (\xi_n - \xi_{n-1}) \\ \Delta S & \mathbf{0}_{1 \times 6} & -I_{1 \times 1} & \mathbf{0}_{1 \times 6} \\ \mathbf{0}_{6 \times 1} & -\mathbf{S}_n^{-1} & -\mathbf{S}_n^{-1} : \mathbf{I}_{6 \times 6} : \boldsymbol{\sigma}_n & -\mathbf{I}_{6 \times 6} \end{bmatrix} \quad \dot{\xi} \neq 0 \\ \left[ \frac{\partial \mathbf{H}_n}{\partial \boldsymbol{\sigma}_n} \right] = \left[ -\mathbf{I}_{6 \times 6} \right] \quad \dot{\xi} = 0 \end{cases} \quad (25)$$

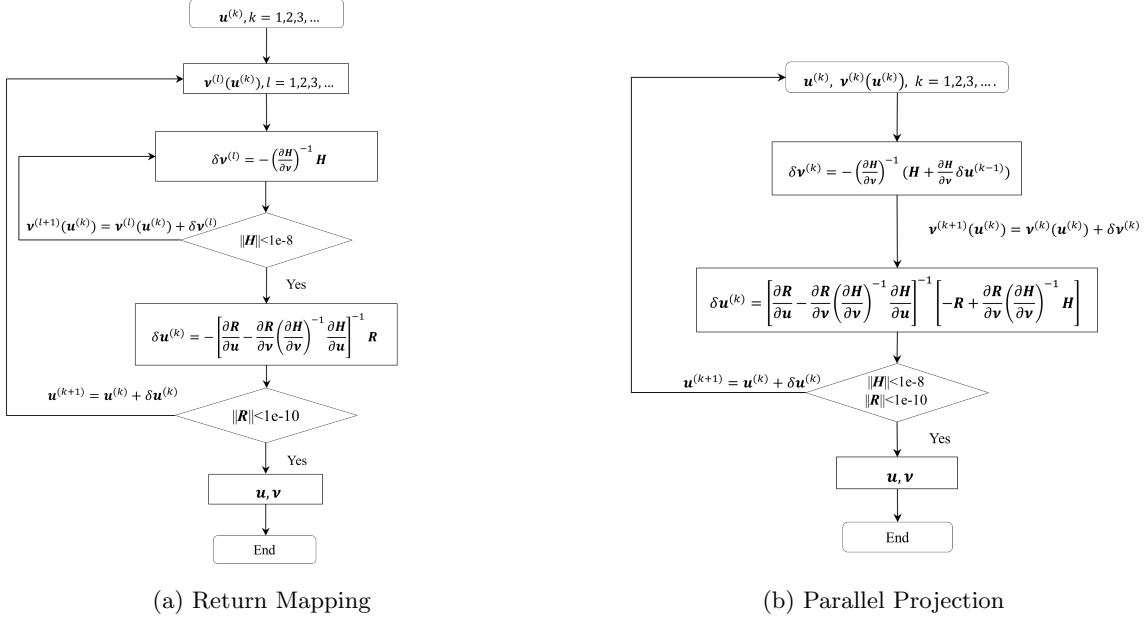


Figure 1: Comparison between the return mapping and parallel projection algorithms

where the superscript  $\text{T}$  denotes the transpose of vectors and matrices.

From Equation 25, we notice that the magnitudes  $S^{-1}$  and  $\mathbf{S}^{-1}$  are much larger than the other internal variables. This results in numerical difficulties in updating the internal state variables, since the matrix  $\partial \mathbf{H} / \partial \boldsymbol{\nu}$  is close to singular. To lessen the effect of the ill-conditioned matrix  $\partial \mathbf{H} / \partial \boldsymbol{\nu}$ , we derive the analytical formula for the internal state variable update  $\delta \boldsymbol{\nu}$  in Equation 21 and 24. To do this, we break the update into two parts. First we compute  $\Delta \boldsymbol{\nu}_{n+1}^{(k)} = -(\partial \mathbf{H}_{n+1}^{(k)} / \partial \boldsymbol{\nu}_{n+1}^{(k)})^{-1} \mathbf{H}_{n+1}^{(k)}$ , which appears in both return mapping and parallel projection algorithms.

$$\Delta \boldsymbol{\nu}_{n+1}^{(k)} = \begin{Bmatrix} \delta \xi_{n+1}^{(k)} \\ \delta \boldsymbol{\varepsilon}_{n+1}^{(k)} \\ \delta S_{n+1}^{(k)} \\ \delta \boldsymbol{\sigma}_{n+1}^{(k)} \end{Bmatrix} = \begin{Bmatrix} \Delta \xi_{n+1}^{*(k)} + \vartheta_{n+1}^{(k)} \\ \Delta \boldsymbol{\varepsilon}_{n+1}^{t*(k)} + \boldsymbol{\Lambda}_{n+1}^{(k)} : \vartheta_{n+1}^{(k)} \\ \Delta S_{n+1}^{*(k)} + H S_{n+1}^{(k)} + \Delta S \cdot \vartheta_{n+1}^{(k)} \\ \Delta \boldsymbol{\sigma}_{n+1}^{*(k)} + \boldsymbol{\xi}_{n+1}^{(k)} : \mathbf{S}_{n+1}^{(k)} : \boldsymbol{\Psi}_{n+1}^{(k)} \end{Bmatrix} \quad (26)$$

where

$$\begin{aligned} \Delta \xi_{n+1}^{*(k)} &= \frac{\Phi_{n+1}^{(k)} - \partial_{\sigma} \Phi_{n+1}^{(k)} : \zeta_{n+1}^{(k)-1} : \mathbf{H} \boldsymbol{\varepsilon}_{n+1}^{(k)}}{\pm \partial_{\sigma} \Phi_{n+1}^{(k)} : \zeta_{n+1}^{(k)-1} : \partial_{\sigma} \Phi_{n+1}^{(k)} - \partial_{\xi} \Phi_{n+1}^{(k)}} & (+ : \dot{\xi} > 0, - : \dot{\xi} < 0) \\ \Delta \boldsymbol{\sigma}_{n+1}^{*(k)} &= \zeta_{n+1}^{(k)-1} : [-\mathbf{H} \boldsymbol{\varepsilon}_{n+1}^{(k)} \mp \Delta \xi_{n+1}^{*(k)} : \partial_{\sigma} \Phi_{n+1}^{(k)}] & (- : \dot{\xi} > 0, + : \dot{\xi} < 0) \\ \Delta \boldsymbol{\varepsilon}_{n+1}^{t*(k)} &= -\mathbf{S}_{n+1}^{(k)} : \Delta \boldsymbol{\sigma}_{n+1}^{*(k)} - [\Delta S : \boldsymbol{\sigma}_{n+1}^{(k)} + \Delta \boldsymbol{\alpha} (T_{n+1} - T_0)] \Delta \xi_{n+1}^{*(k)} & (27) \\ \Delta S_{n+1}^{*(k)} &= \Delta S \Delta \xi_{n+1}^{*(k)} \\ \boldsymbol{\Psi}_{n+1}^{(k)} &= \mathbf{H} \boldsymbol{\sigma}_{n+1}^{(k)} - S_{n+1}^{(k)-1} : \mathbf{I} : \boldsymbol{\sigma}_{n+1}^{(k)} : H S_{n+1}^{(k)} \\ \vartheta_{n+1}^{(k)} &= \frac{\partial_{\sigma} \Phi_{n+1}^{(k)}}{\pm \partial_{\sigma} \Phi_{n+1}^{(k)} : \zeta_{n+1}^{(k)-1} : \partial_{\sigma} \Phi_{n+1}^{(k)} - \partial_{\xi} \Phi_{n+1}^{(k)}} : \zeta_{n+1}^{(k)-1} : \mathbf{S}_{n+1}^{(k)} : \boldsymbol{\Psi}_{n+1}^{(k)} & (+ : \dot{\xi} > 0, - : \dot{\xi} < 0) \end{aligned}$$



$$\zeta_{n+1}^{(k)} = \begin{cases} \mathbf{S}_{n+1}^{(k)} + \partial_{\sigma} \mathbf{\Lambda}_{n+1}^{(k)} : (\xi_{n+1}^{(k)} - \xi_n) & \dot{\xi} > 0 \\ \mathbf{S}_{n+1}^{(k)} & \dot{\xi} < 0 \end{cases}$$

Next we evaluate  $\Delta \boldsymbol{\nu}_{n+1}^{*(k)} = -(\partial \mathbf{H}_{n+1}^{(k)} / \partial \boldsymbol{\nu}_{n+1}^{(k)})^{-1} (\partial \mathbf{H}_{n+1}^{(k)} / \partial \mathbf{u}_{n+1}^{(k)}) \delta \mathbf{u}_{n+1}^{(k-1)}$ , which only appears in the parallel projection algorithm. The analytical solution of it can be derived as,

$$\Delta \boldsymbol{\nu}_{n+1}^{*(k)} = \left[ \begin{array}{c} \frac{\partial_{\sigma} \Phi_{n+1}^{(k) \text{ T}} : \zeta_{n+1}^{(k) -1}}{\pm \partial_{\sigma} \Phi_{n+1}^{(k)} : \zeta_{n+1}^{(k) -1} : \partial_{\sigma} \Phi_{n+1}^{(k)} - \partial_{\xi} \Phi_{n+1}^{(k)}} \\ \frac{\tilde{\mathbf{\Lambda}}_{n+1}^{(k)} : \partial_{\sigma} \Phi_{n+1}^{(k) \text{ T}}}{\pm \partial_{\sigma} \Phi_{n+1}^{(k)} : \zeta_{n+1}^{(k) -1} : \partial_{\sigma} \Phi_{n+1}^{(k)} - \partial_{\xi} \Phi_{n+1}^{(k)}} : \zeta_{n+1}^{(k) -1} + \mathbf{S}_{n+1}^{(k)} : \zeta_{n+1}^{(k) -1} - \mathbf{I}_{6 \times 6} \\ \frac{\Delta S : \partial_{\sigma} \Phi_{n+1}^{(k) \text{ T}}}{\pm \partial_{\sigma} \Phi_{n+1}^{(k)} : \zeta_{n+1}^{(k) -1} : \partial_{\sigma} \Phi_{n+1}^{(k)} - \partial_{\xi} \Phi_{n+1}^{(k)}} : \zeta_{n+1}^{(k) -1} \\ \mathfrak{L}_{n+1}^{(k-1)} \end{array} \right] \mathbf{B} : \delta \mathbf{u}_{n+1}^{(k-1)} \quad (28)$$

where we use + if  $\dot{\xi} > 0$  and - if  $\dot{\xi} < 0$ , and define

$$\tilde{\mathbf{\Lambda}}_{n+1}^{(k)} = \mathbf{S}_{n+1}^{(k)} : \zeta_{n+1}^{(k) -1} : (\mathbf{\Lambda}_{n+1}^{(k)} - \partial_{\sigma} \mathbf{\Lambda}_{n+1}^{(k)} : \Delta \xi_{n+1}^{(k)} : \mathbf{S}_{n+1}^{(k) -1} : \mathbf{I}_{6 \times 6} : \sigma_{n+1}^{(k)} : \Delta S) \quad (29)$$

Note that during the inverse transformation, i.e.  $\dot{\xi} < 0$ ,  $\tilde{\mathbf{\Lambda}}_{n+1}^{(k)}$  degenerates to the transformation tensor  $\mathbf{\Lambda}_{n+1}^{(k)}$ , since  $\zeta_{n+1}^{(k)} = \mathbf{S}_{n+1}^{(k)}$  and  $\partial_{\sigma} \mathbf{\Lambda}_{n+1}^{(k)} = 0$ . Ultimately, the local Newton-Raphson updated increment  $\delta \boldsymbol{\nu}_n^{(k+1)}$  shown in Equations 21 and 24 can be evaluated as

$$\delta \boldsymbol{\nu}_{n+1}^{(k+1)} = \begin{cases} \Delta \boldsymbol{\nu}_{n+1}^{(k)} & \text{(Return Mapping)} \\ \Delta \boldsymbol{\nu}_{n+1}^{(k)} + \Delta \boldsymbol{\nu}_{n+1}^{*(k)} & \text{(Parallel Projection)} \end{cases} \quad (30)$$

A detailed derivation of these quantities is provided in Appendix A.

With these formulas, we can also obtain the consistent tangent stiffness modulus  $\mathfrak{L}_{n+1}^{(k)}$  to update the displacement, i.e.  $(\partial \mathbf{R} / \partial \mathbf{u}) - (\partial \mathbf{R} / \partial \boldsymbol{\nu})(\partial \mathbf{H} / \partial \boldsymbol{\nu})^{-1} (\partial \mathbf{H} / \partial \mathbf{u}) = \sum_{\text{G}} w \mathbf{B}^{\text{T}} \mathfrak{L}_{n+1}^{(k)} \mathbf{B} \det \mathbf{J}$ , where  $\mathfrak{L}_{n+1}^{(k)}$  has the form as

$$\mathfrak{L}_{n+1}^{(k)} = \zeta_{n+1}^{(k) -1} - \frac{\zeta_{n+1}^{(k) -1} : \partial_{\sigma} \Phi_{n+1}^{(k)} \otimes \zeta_{n+1}^{(k) -1} : \partial_{\sigma} \Phi_{n+1}^{(k)}}{\partial_{\sigma} \Phi_{n+1}^{(k)} : \zeta_{n+1}^{(k) -1} : \partial_{\sigma} \Phi_{n+1}^{(k)} \mp \partial_{\xi} \Phi_{n+1}^{(k)}} \quad (+ : \dot{\xi} > 0, - : \dot{\xi} < 0) \quad (31)$$

and  $\zeta_n$  is defined in Equation 27. Note the similarity in the form of the "continuum" tangent operator of Equation 17 and the "consistent" tangent operator of 31.

Now, we contextualize our Newton-Raphson updating scheme for the local residual  $\mathbf{H}$  with the popular radial return [31], closest-point [33] and cutting plane methods [14]. The Newton-Raphson scheme can be simplified by strictly enforcing some of the local residual equations in  $\mathbf{H} = [H_{\phi}, \mathbf{H}_{\varepsilon^t}, H_S, \mathbf{H}_{\sigma}]^{\text{T}} = 0$  to eliminate their associated internal variables  $\xi, \varepsilon^t, S, \sigma$ , ct. Table 1.

Newton-Raphson Method	Radial return Method
	Strictly enforced : $\mathbf{H}_\sigma = 0$ to eliminate $\sigma$
Increment : $\delta\xi_{n+1}^{(k)} = \Delta\xi_{n+1}^{*(k)} + \vartheta_{n+1}^{(k)}$ $\delta\varepsilon_{n+1}^{t(k)} = \Delta\varepsilon_{n+1}^{t*(k)} + \mathbf{\Lambda}_{n+1}^{(k)} : \vartheta_{n+1}^{(k)}$ $\delta S_{n+1}^{(k)} = \Delta S_{n+1}^{*(k)} + H S_{n+1}^{(k)} + \Delta S \cdot \vartheta_{n+1}^{(k)}$ $\delta\sigma_{n+1}^{(k)} = \Delta\sigma_{n+1}^{*(k)} + \mathbf{\xi}_{n+1}^{(k)} : \mathbf{S}_{n+1}^{(k)} : \Psi_{n+1}^{(k)}$ Consistent tangent operator : $\mathbf{\xi}_n = \begin{cases} \zeta_n^{-1} - \frac{\zeta_n^{-1} : \partial_\sigma \Phi_n \otimes \zeta_n^{-1} : \partial_\sigma \Phi_n}{\partial_\sigma \Phi_n : \zeta_n^{-1} : \partial_\sigma \Phi_n - \partial_\xi \Phi_n} & \dot{\xi} > 0 \\ \mathbf{S}_n^{-1} - \frac{\mathbf{S}_n^{-1} : \partial_\sigma \Phi_n \otimes \mathbf{S}_n^{-1} : \partial_\sigma \Phi_n}{\partial_\sigma \Phi_n : \mathbf{S}_n^{-1} : \partial_\sigma \Phi_n + \partial_\xi \Phi_n} & \dot{\xi} < 0 \end{cases}$	Increment : $\delta\xi_{n+1}^{(k)} = \Delta\xi_{n+1}^{*(k)} + \vartheta_{n+1}^{(k)}$ $\delta\varepsilon_{n+1}^{t(k)} = \Delta\varepsilon_{n+1}^{t*(k)} + \mathbf{\Lambda}_{n+1}^{(k)} : \vartheta_{n+1}^{(k)}$ $\delta S_{n+1}^{(k)} = \Delta S_{n+1}^{*(k)} + H S_{n+1}^{(k)} + \Delta S \cdot \vartheta_{n+1}^{(k)}$ $\vartheta_{n+1}^{(k)} = \frac{\partial_\sigma \Phi_{n+1}^{(k)} : \zeta_{n+1}^{(k)-1} : \mathbf{S}_{n+1}^{(k)} : (-S_{n+1}^{(k)-1} : \sigma_{n+1}^{(k)} : H S_{n+1}^{(k)})}{\pm \partial_\sigma \Phi_{n+1}^{(k)} : \zeta_{n+1}^{(k)-1} : \partial_\sigma \Phi_{n+1}^{(k)} - \partial_\xi \Phi_{n+1}^{(k)}}$ $\sigma_{n+1}^{(k+1)} = \mathbf{S}_{n+1}^{(k+1)-1} : [\varepsilon_{n+1} - \alpha(T_{n+1} - T_0) - \varepsilon_{n+1}^{t(k+1)}]$ Consistent tangent operator : $\mathbf{\xi}_n = \begin{cases} \zeta_n^{-1} - \frac{\zeta_n^{-1} : \partial_\sigma \Phi_n \otimes \zeta_n^{-1} : \partial_\sigma \Phi_n}{\partial_\sigma \Phi_n : \zeta_n^{-1} : \partial_\sigma \Phi_n - \partial_\xi \Phi_n} & \dot{\xi} > 0 \\ \mathbf{S}_n^{-1} - \frac{\mathbf{S}_n^{-1} : \partial_\sigma \Phi_n \otimes \mathbf{S}_n^{-1} : \partial_\sigma \Phi_n}{\partial_\sigma \Phi_n : \mathbf{S}_n^{-1} : \partial_\sigma \Phi_n + \partial_\xi \Phi_n} & \dot{\xi} < 0 \end{cases}$
Closest-Point Method [33]	Cutting Plane Method[14]
Strictly enforced : $H_S = 0$ , $\mathbf{H}_\sigma = 0$ to eliminate $S$ and $\sigma$	Strictly enforced : $H_S = 0$ , $\mathbf{H}_{\varepsilon^t} = 0$ , $\mathbf{H}_\sigma = 0$ to eliminate $S$ , $\varepsilon^t$ and $\sigma$
Increment : $\delta\xi_{n+1}^{(k)} = \Delta\xi_{n+1}^{*(k)}$ $\delta\varepsilon_{n+1}^{t(k)} = \Delta\varepsilon_{n+1}^{t*(k)}$ $\delta S_{n+1}^{(k)} = \Delta S \Delta\xi_{n+1}^{*(k)}$ $\sigma_{n+1}^{(k+1)} = \mathbf{S}_{n+1}^{(k+1)-1} : [\varepsilon_{n+1} - \alpha(T_{n+1} - T_0) - \varepsilon_{n+1}^{t(k+1)}]$ Consistent tangent operator : $\mathbf{\xi}_n = \begin{cases} \zeta_n^{-1} - \frac{\zeta_n^{-1} : \partial_\sigma \Phi_n \otimes \zeta_n^{-1} : \partial_\sigma \Phi_n}{\partial_\sigma \Phi_n : \zeta_n^{-1} : \partial_\sigma \Phi_n - \partial_\xi \Phi_n} & \dot{\xi} > 0 \\ \mathbf{S}_n^{-1} - \frac{\mathbf{S}_n^{-1} : \partial_\sigma \Phi_n \otimes \mathbf{S}_n^{-1} : \partial_\sigma \Phi_n}{\partial_\sigma \Phi_n : \mathbf{S}_n^{-1} : \partial_\sigma \Phi_n + \partial_\xi \Phi_n} & \dot{\xi} < 0 \end{cases}$	Increment : $\delta\xi_{n+1}^{(k)} = \frac{\Phi_{n+1}^{(k)}}{\pm \partial_\sigma \Phi_{n+1}^{(k)} : \mathbf{S}_{n+1}^{(k)-1} : \partial_\sigma \Phi_{n+1}^{(k)} - \partial_\xi \Phi_{n+1}^{(k)}}$ $\delta\varepsilon_{n+1}^{t(k)} = \mathbf{\Lambda}_{n+1}^{(k)} : \delta\xi_{n+1}^{(k)}$ $\delta S_{n+1}^{(k)} = \Delta S \delta\xi_{n+1}^{(k)}$ $\sigma_{n+1}^{(k)} = \mathbf{S}_{n+1}^{(k+1)-1} : [\varepsilon_{n+1} - \alpha(T_{n+1} - T_0) - \varepsilon_{n+1}^{t(k+1)}]$ Consistent tangent operator : $\mathbf{\xi}_n = \begin{cases} \mathbf{S}_n^{-1} - \frac{\mathbf{S}_n^{-1} : \partial_\sigma \Phi_n \otimes \mathbf{S}_n^{-1} : \partial_\sigma \Phi_n}{\partial_\sigma \Phi_n : \mathbf{S}_n^{-1} : \partial_\sigma \Phi_n - \partial_\xi \Phi_n} & \dot{\xi} > 0 \\ \mathbf{S}_n^{-1} - \frac{\mathbf{S}_n^{-1} : \partial_\sigma \Phi_n \otimes \mathbf{S}_n^{-1} : \partial_\sigma \Phi_n}{\partial_\sigma \Phi_n : \mathbf{S}_n^{-1} : \partial_\sigma \Phi_n + \partial_\xi \Phi_n} & \dot{\xi} < 0 \end{cases}$

Table 1: Comparison of techniques to update internal state variables in  $\Delta v$

We can also strictly enforce particular residuals in the parallel projection algorithm. Summarizing all of the above methods, i.e. the Newton-Raphson, radial return, closest-point and cutting plane methods, are applicable to both the return mapping and parallel projection algorithms. The difference being that local iterations are performed in the return mapping algorithm, but not in the parallel projection algorithm.

To better understand the implementation of the parallel projection algorithm, and its ability to be combined with various local updating techniques, we provide a pseudo-code implementation of it with the closest-point updating technique in the Table 2.

---

**initialization:** initialize external and internal state variables at pseudo-time step  $n + 1$

---

I. Let  $k = 1, T_{n+1} = T_n + n \cdot dT, \mathbf{F}_{n+1} = \mathbf{F}_n + n \cdot d\mathbf{F}, \mathbf{d}_{n+1}^{(1)} = \mathbf{d}_n$

$$\xi_{n+1}^{(1)} = \xi_n, \varepsilon_{n+1}^{t(1)} = \varepsilon_n^t, S_{n+1}^{(1)} = S_n$$

II. Loop over Gauss points, calculate total strain  $\varepsilon_{n+1}^{(k)} = \mathbf{B} \mathbf{d}_{n+1}^{(k)}$  and go to inner loop

---

**Inner Update:** Update internal state variables for one iteration step

---

1. Calculate trial stress  $\boldsymbol{\sigma}_{n+1}^{(k)}$  using  $S_{n+1}^{(k)}$ ,  $\boldsymbol{\varepsilon}_{n+1}^{(k)}$  and  $\boldsymbol{\varepsilon}_{n+1}^t(k)$  from previous iteration, and evaluate the local residual  $\mathbf{H}^{(k)} = [H_{\Phi}^{(k)}, \mathbf{H}_{\boldsymbol{\varepsilon}^t}^{(k)}]$

$$\boldsymbol{\sigma}_{n+1}^{(k)} = \mathbf{S}_{n+1}^{(k)-1} : [\boldsymbol{\varepsilon}_{n+1}^{(k)} - \alpha(T_{n+1} - T_0) - \boldsymbol{\varepsilon}_{n+1}^t(k)]$$

$$H_{\Phi}^{(k)} = \Phi[\boldsymbol{\sigma}_{n+1}^{(k)}, T_{n+1}, \xi_{n+1}^{(k)}]$$

$$\mathbf{H}_{\boldsymbol{\varepsilon}^t}^{(k)} = \boldsymbol{\varepsilon}_n^t + \boldsymbol{\Lambda}_{n+1}^{(k)}[\xi_{n+1}^{(k)} - \xi_n] - \boldsymbol{\varepsilon}_{n+1}^t(k)$$

$$\text{If } |H_{\Phi}^{(k)}| \leq e_1^H \text{ and } \|\mathbf{H}_{\boldsymbol{\varepsilon}^t}^{(k)}\| \leq e_2^H$$

Compute consistent tangent stiffness modulus  $\boldsymbol{\mathfrak{L}}^{(k+1)}$ , update internal variables with the current values and go to Outer Loop

Else

Continue to step 2

2. Compute increment of inner state variables  $-(\partial\mathbf{H}/\partial\boldsymbol{\nu})^{-1}\mathbf{H}$

$$\delta\xi_{n+1}^{(k)} = \frac{\Phi_{n+1}^{(k)} - \partial_{\sigma}\Phi_{n+1}^{(k)} : \mathbf{S}_{n+1}^{(k)-1} : \mathbf{H}_{\boldsymbol{\varepsilon}^t}}{\pm\partial_{\sigma}\Phi_{n+1}^{(k)} : \mathbf{S}_{n+1}^{(k)-1} : \partial_{\sigma}\Phi_{n+1}^{(k)} - \partial_{\xi}\Phi_{n+1}^{(k)}} \quad (+ : \dot{\xi} > 0, - : \dot{\xi} < 0)$$

$$\Delta\boldsymbol{\sigma}_{n+1}^{*(k)} = \mathbf{S}_{n+1}^{(k)-1} : [-H_{\boldsymbol{\varepsilon}^t} \mp \Delta\xi_{n+1}^{(k)} \partial_{\sigma}\Phi_{n+1}^{(k)}] \quad (- : \dot{\xi} > 0, + : \dot{\xi} < 0)$$

$$\delta\boldsymbol{\varepsilon}_{n+1}^t(k) = -\mathbf{S}_{n+1}^{(k)} : \Delta\boldsymbol{\sigma}_{n+1}^{*(k)} - [\Delta\mathbf{S} : \boldsymbol{\sigma}_{n+1}^{(k)} + \Delta\alpha(T_{n+1} - T_0)]\delta\xi_{n+1}^{(k)}$$

3. Update martensite volume fraction, transformation strain and compliance modulus

$$\xi_{n+1}^{(k+1)} = \xi_{n+1}^{(k)} + \delta\xi_{n+1}^{(k)}$$

$$\boldsymbol{\varepsilon}_{n+1}^t(k+1) = \boldsymbol{\varepsilon}_{n+1}^t(k) + \delta\boldsymbol{\varepsilon}_{n+1}^t(k)$$

$$S_{n+1}^{(k+1)} = S_{n+1}^{(k)} + \Delta S \delta\xi_{n+1}^{(k)}$$

$$\boldsymbol{\sigma}_{n+1}^{(k+1)} = \mathbf{S}_{n+1}^{(k+1)-1} : [\boldsymbol{\varepsilon}_{n+1}^{(k)} - \alpha(T_{n+1} - T_0) - \boldsymbol{\varepsilon}_{n+1}^t(k+1)]$$

4. Compute consistent tangent stiffness modulus  $\boldsymbol{\mathfrak{L}}^{(k)}$  and go to Outer Update

---

**Outer Update:** Update displacement

---

- III. Assemble global tangent stiffness matrix  $\mathbf{K}$ , internal force  $\mathbf{F}_{int}$

$$\mathbf{K} = \bigwedge_{\text{el}} \sum_{\text{G}} w \mathbf{B}_{\text{G}}^T \boldsymbol{\mathfrak{L}}_{\text{G}}^{(k)} \mathbf{B}_{\text{G}} \det \mathbf{J}_{\text{G}}, \mathbf{F}_{int}^{(k)} = \bigwedge_{\text{el}} \sum_{\text{G}} \varpi \mathbf{B}_{\text{G}}^T \boldsymbol{\sigma}_{\text{G}}^{(k)} \det \mathbf{J}_{\text{G}}$$

- IV. Calculate the global residual

$$\mathbf{R}^{(k)} = \mathbf{F}_{int}^{(k)} - \mathbf{F}_{n+1}$$

- V. Evaluate the convergence condition

$$\text{If } \|\mathbf{R}^{(k)}\| \leq e^R \text{ and for all Gaussian points } \|\mathbf{H}_{\text{G}}^{(k)}\| \leq e_{\text{G}}^H$$

Finalize the external variables  $\mathbf{u}_{n+1}$  and internal variables  $\boldsymbol{\nu}_{n+1}$

Let  $n = n + 1$ , return to step I until the end of pseudo-time step

Else

$$\text{Update the displacement field, } \mathbf{d}_{n+1}^{(k+1)} = \mathbf{d}_{n+1}^{(k)} - \mathbf{K}^{-1} \left[ \mathbf{R}^{(k)} + \frac{\partial \mathbf{R}}{\partial \boldsymbol{\nu}} \left( \frac{\partial \mathbf{H}}{\partial \boldsymbol{\nu}} \right)^{-1} \mathbf{H}^{(k)} \right]$$

Let  $k = k + 1$ , return to Inner Update

---

Table 2: Parallel projection — closest-point algorithm.

### 3. Example Problems

To illustrate the capability of the parallel projection algorithm and the newly developed updating scheme for the local residuals, various simulations of TWSMEs and superelasticity of SMAs are provided. All of the simulations are based on NiTi50, whose properties are provided in Table 3. The finite element analysis in all cases is carried out via the parallel projection and return mapping algorithms. For both algorithms, the global residual  $\mathbf{R}$  convergence tolerance is  $e_{\mathbf{R}} = 10^{-6}$ , and the local residual  $\mathbf{H}$  convergence tolerance is  $e_{\mathbf{H}} = 10^{-6}$ . The simulations are conducted via com-

mercial software MATLAB(R) 2016b, on a workstation platform equipped with an Intel(R) Core i5-6500 CPU and 8GB memory (RAM).

	Austenite (A)	Martensite (M)
Young's modulus $E$ (Pa)	$32.5 \times 10^9$	$23.0 \times 10^9$
Thermal coefficient $\alpha$ ( $\text{K}^{-1}$ )	$22.0 \times 10^{-6}$	$22.0 \times 10^{-6}$
Specific heat $c$ (J/kgK)	400.0	400.0
Transformation start temperature $A_s$ and $M_s$ (K)	241	226
Transformation finish $A_f$ and $M_f$ temperature (K)	290	194
Highest transformation strain $H$	0.033	
Material density $\rho$ ( $\text{kg}/\text{m}^3$ )	6500	
Reference temperature $T_0$ (K)	300	
Entropy difference $\rho\Delta s_0$ ( $\text{J}/\text{m}^3\text{K}$ )	$-11.55 \times 10^4$	

Table 3: Material properties of NiTi50

### 3.1. 1D SMA Problem

We start the discussion with 1D SMA problems, because their constitutive model can be analytically solved, which enables a direct verification of different algorithms. The boundary conditions and parameters of the simulated 1D bar are shown in Figure 2. The length of the structures is divided into a mesh of ten equally-sized bar finite elements, with a cross section of  $0.1\text{m}^2$ .

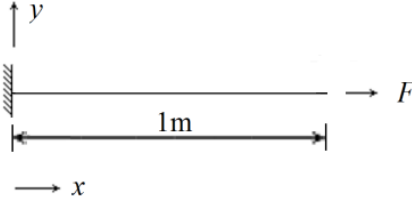


Figure 2: Boundary conditions for the 1D bar problem with various hardening models

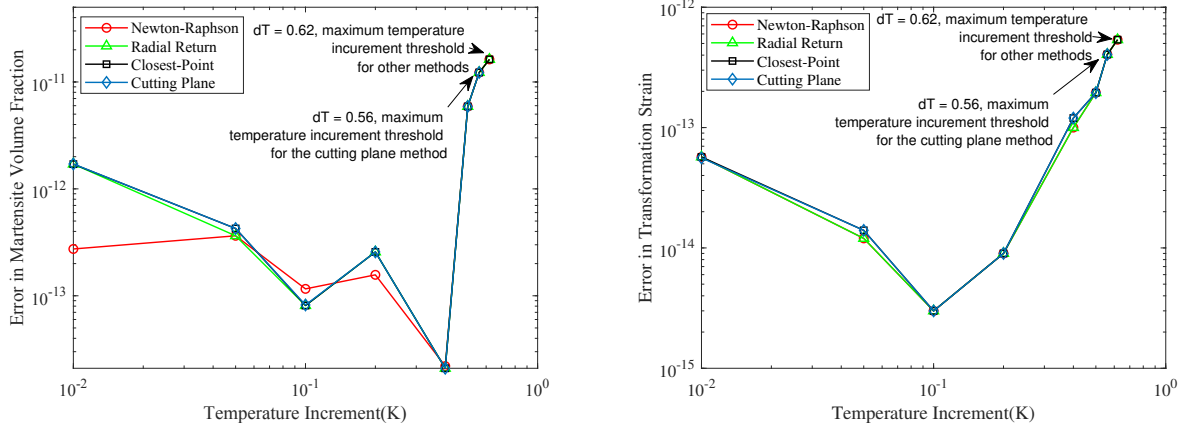
For the simulation of TWSME, a temperature cycle ranging from 180 to 300K is applied to the structure; the structure is stress free as no external loads are applied. When simulating the superelasticity of SMAs, the structure is subjected to an axial loading cycle ranging from  $5 \times 10^6\text{N}$  to  $5 \times 10^9\text{N}$ , at a uniform temperature 310K. Note that the phase transformation evolves uniformly, since the structure undergoes uniaxial stress.

#### 3.1.1. Accuracy of Local Residual Updating Scheme Implemented in the Parallel Projection Algorithm

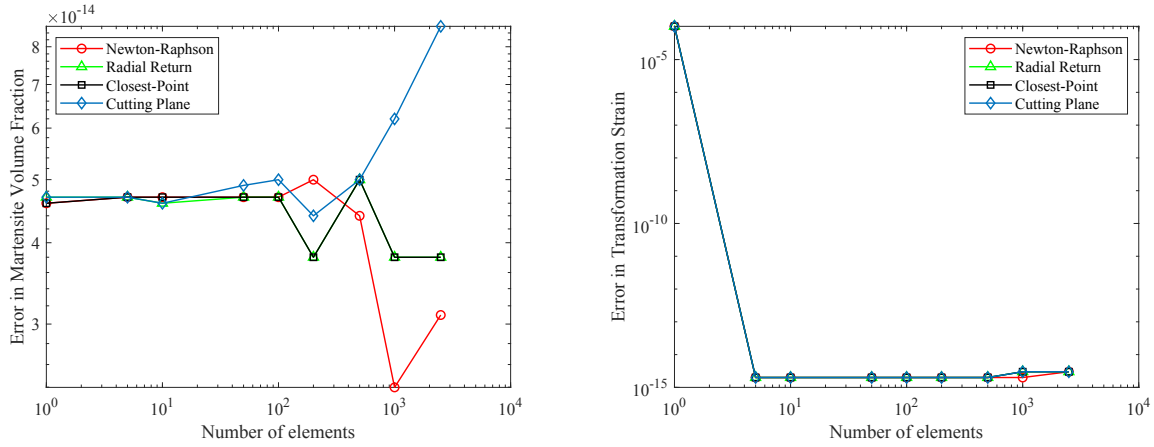
To compare the accuracy and stability of the four different updating schemes for local residuals, i.e the Newton Raphson, radio return, closest-point and cutting plane methods, we compare the their convergences when embedded in the return mapping and parallel projection algorithms, cf. Figures 3 and 4. The comparison is conducted in the TWSME case with the analytic solution [14]

$$\begin{aligned}
 \xi &= \frac{1}{\rho b^M} [|\sigma|H + \frac{1}{2}\Delta S\sigma^2 + \rho\Delta s_0(T - M_s)] \\
 \varepsilon^t &= \frac{H\text{sgn}(\sigma)}{\rho b^M} [|\sigma|H + \frac{1}{2}\Delta S\sigma^2 + \rho\Delta s_0(T - M_s)]
 \end{aligned} \tag{32}$$

which uses the quadratic polynomial hardening function, and  $b^M = -\Delta s_0(M_s - M_f)$ . The convergences are compared at the temperature of 220K.

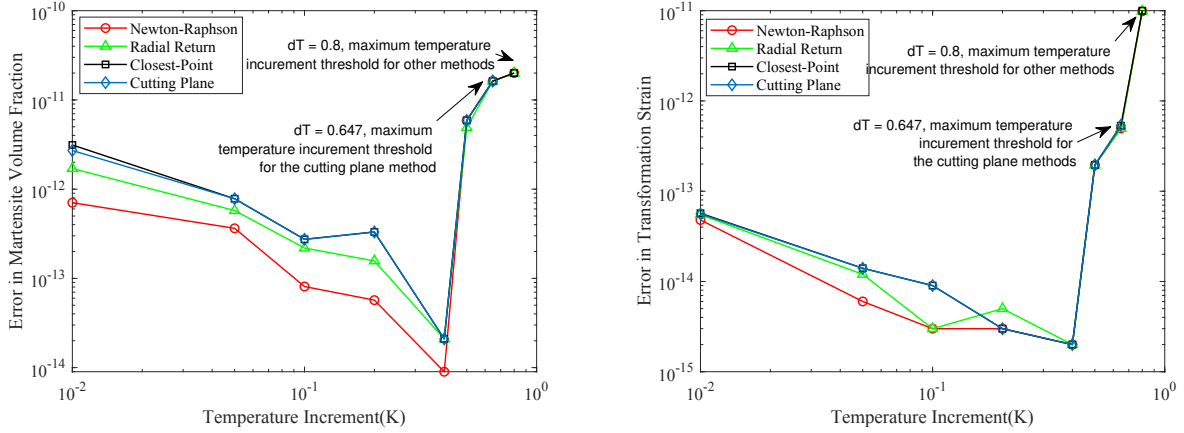


(a) Error vs. temperature increment

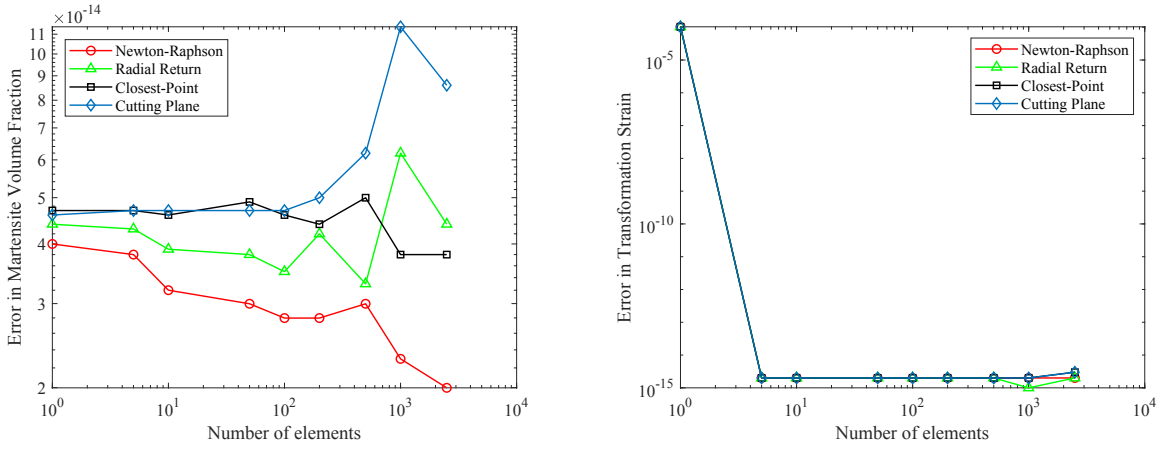


(b) Error vs. number of elements

Figure 3: Error between the 1D analytic solution and different return mapping schemes for updating internal state variables at  $T = 220\text{K}$



(a) Error vs. temperature increment



(b) Error vs. number of elements

Figure 4: Error between the 1D analytic solution and different parallel projection schemes for updating internal state variables at  $T = 220\text{K}$

In Figure 3a and 4a, the arrow refers to the maximum temperature increment that we can use with the each method to attain convergence. These methods solve the same equations but their radii of convergence vary. Indeed, as seen in Figures 3 and 4, eliminating variables hinders the convergence. In addition, we also notice that the parallel projection algorithm generally allows for larger temperature increments than the return mapping algorithm which strictly enforces the residual equation  $\mathbf{H} = 0$  at each global iteration. This finding is consistent in simulating the superelasticity, cf. Table 4

Methods	Newton-Raphson	Radial Return	Closest-Point	Cutting Plane
Return Mapping	$9 \times 10^8\text{N}$	$9 \times 10^8\text{N}$	$9 \times 10^8\text{N}$	$9 \times 10^8\text{N}$
Parallel Projection	$3 \times 10^9\text{N}$	$3 \times 10^9\text{N}$	$3 \times 10^9\text{N}$	$3 \times 10^9\text{N}$

Table 4: Approximate maximum loading step for simulating superelasticity

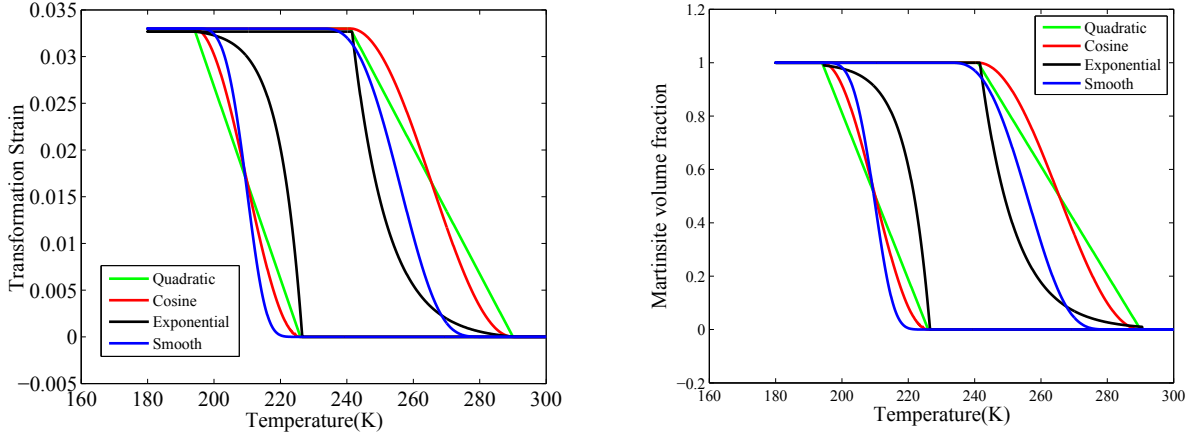
### 3.1.2. Adaptability of the Parallel Projection Algorithm with Various Constitutive Models

To demonstrate that the Parallel Projection algorithm is able to handle different constitutive relationships (i.e. hardening models) of SMAs, we repeat the above study. However, we only use

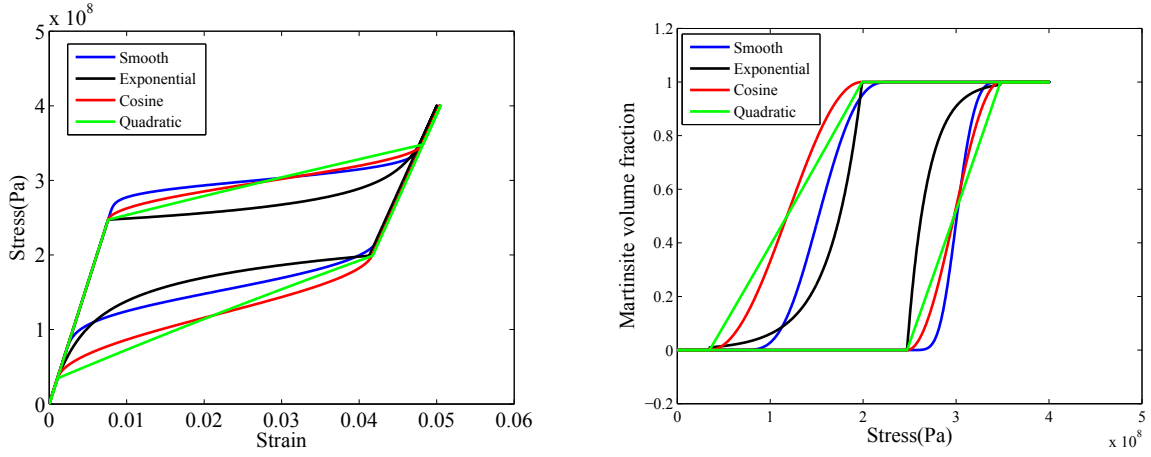
the cloest point scheme and replace the hardening function ( $f$ ) with the most popular models proposed in the past two decades. Due to differences in fitting techniques for Differential Scanning Calorimetry (DSC)-obtained experimental data [12], various hardening functions have been created to model the hysteresis curve of TWSMEs and superelasticity. These models, cf. Equation 33, include the quadratic model proposed by Lagoudas [14], the cosine model proposed by Liang [10, 11], the exponential model proposed by Tanaka [9], and the smooth model proposed by Lagoudas [14].

$$\begin{aligned}
\text{Quadratic : } f(\xi) &= \begin{cases} \frac{1}{2}\rho b^M \xi^2 + (\mu_1 + \mu_2)\xi & (\dot{\xi} > 0) \\ \frac{1}{2}\rho b^A \xi^2 + (\mu_1 - \mu_2)\xi & (\dot{\xi} < 0) \end{cases} \\
\text{Cosine : } f(\xi) &= \begin{cases} \int_{\xi}^0 -\frac{\rho\Delta s_0}{a_c^M} [\pi - \cos^{-1}(2\xi - 1)]d\xi + (\mu_1^c + \mu_2^c)\xi & (\dot{\xi} > 0) \\ \int_{\xi}^0 -\frac{\rho\Delta s_0}{a_c^A} [\pi - \cos^{-1}(2\xi - 1)]d\xi + (\mu_1^c - \mu_2^c)\xi & (\dot{\xi} < 0) \end{cases} \quad (33) \\
\text{Exponential : } f(\xi) &= \begin{cases} \frac{\rho\Delta s_0}{a_e^M} [(1 - \xi) \ln(1 - \xi) + \xi] + (\mu_1^e + \mu_2^e)\xi & (\dot{\xi} > 0) \\ -\frac{\rho\Delta s_0}{a_e^A} [\xi \ln(\xi) - \xi] + (\mu_1^e - \mu_2^e)\xi & (\dot{\xi} < 0) \end{cases} \\
\text{Smooth : } f(\xi) &= \begin{cases} \frac{1}{2}\rho b^M \left[ \xi + \frac{\xi^{n_1+1}}{n_1+1} + \frac{(1-\xi)^{n_2+1}}{n_2+1} \right] & (\dot{\xi} > 0) \\ \frac{1}{2}\rho b^A \left[ \xi + \frac{\xi^{n_3+1}}{n_3+1} + \frac{(1-\xi)^{n_4+1}}{n_4+1} \right] & (\dot{\xi} < 0) \end{cases}
\end{aligned}$$

the parameters  $a, b, n$  and  $\mu$  in Equation 33, are defined in [14]. In Figure 5, we present the results of the evolution of strain and martensite volume fraction under a temperature cycle, and the evolution of stress and martensite volume fraction under a loading cycle, of the Gauss point of the first (left-most) element, respectively.



(a) Two-way shape memory effect



(b) Superelasticity

Figure 5: Simulating TWSMEs and superelasticity with the parallel projection algorithm using different hardening models

These results agree with the return mapping computations and the analytical solutions presented in [14].

### 3.2. 3D SMA Examples

#### 3.2.1. Computation Efficiency of the Parallel Projection Algorithm in 3D Problem

In this section, we compare the parallel projection algorithm with the return mapping algorithm in a 3D simulation, to exemplify the computation efficiency of the parallel projection algorithm. The 3D SMA bar that is meshed with  $2 \times 10 \times 2$  hexahedral elements, is subject to a coupled temperature and mechanical loading cycle, with amplitude ranges  $210 \sim 310\text{K}$  and  $2 \times 10^6 \sim 2.2 \times 10^7\text{N/m}^2$ . cf. Figure 6



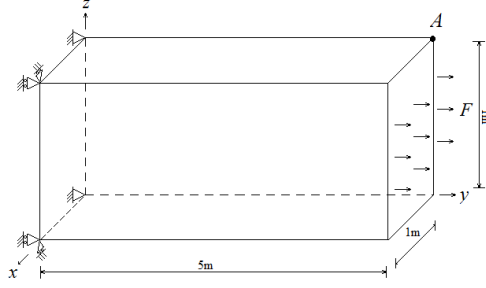


Figure 6: Geometry and boundary conditions of the 3D SMA bar

In Figure 7, we can see that the bar deforms in all three directions.

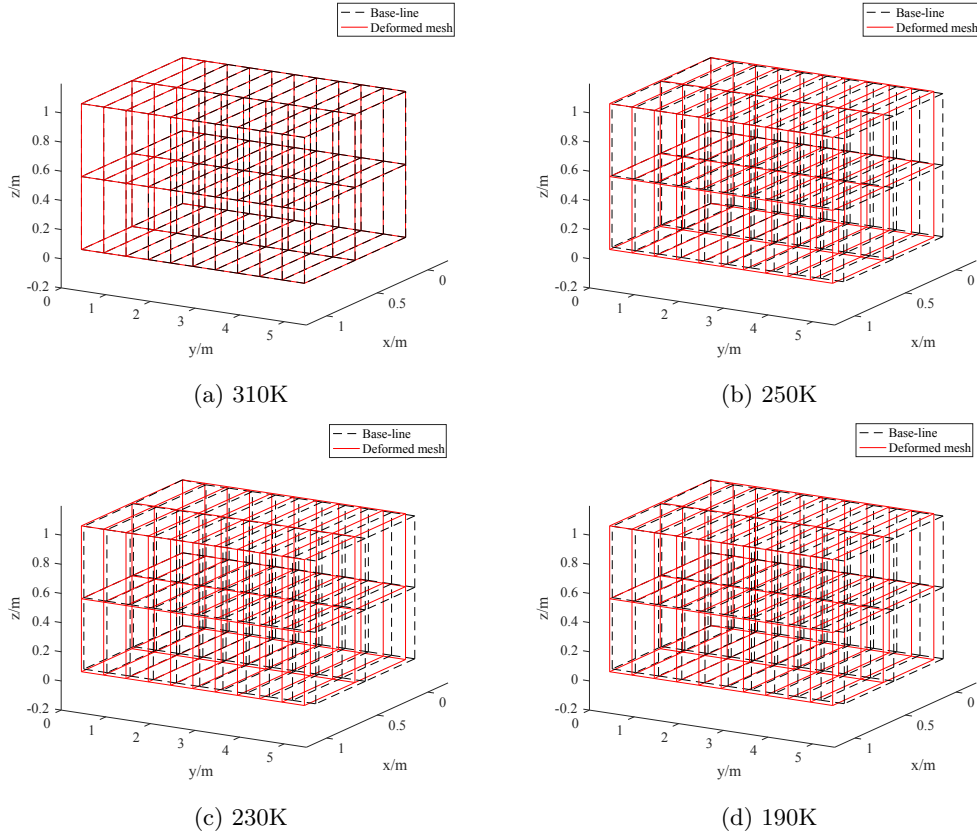


Figure 7: Deformation of a 3D bar under coupled thermomechanical loading

Figure 8 compares evolution of the total strain  $\epsilon_{xx}^{G_A}$ , stress  $\sigma_{xx}^{G_A}$  and martensite volume fraction  $\xi_{G_A}$  for the two methods. Here, point  $A$  is the right tip point of the structure, shown in Figure 6.  $G_A$  is the closest Gauss point to the point  $A$ . Note that the phase transformation is influenced by both the temperature and stress. From the results, we see an ideal match between the parallel projection and return mapping computations. Figure 9 shows the convergence rate of the global residual  $\mathbf{R}$  at thermomechanical loading step size of  $dT = 0.1\text{K}$  and  $dF = 1 \times 10^5\text{N/m}^2$ . It is observed that the radius of quadratic convergence of the return mapping algorithm is adversely influenced due to enforcing  $\mathbf{H}$  to zero at each outer iteration. We also noticed that while all four methods exhibit quadratic convergence for the parallel projection algorithm, the variation of their radii of convergence explains the divergence observed in the 1D problem. Based on our testings,

we suggest using a line-search method to deal with such divergence, as proposed for implementing the cutting plane method in plasticity simulation [31, 36].

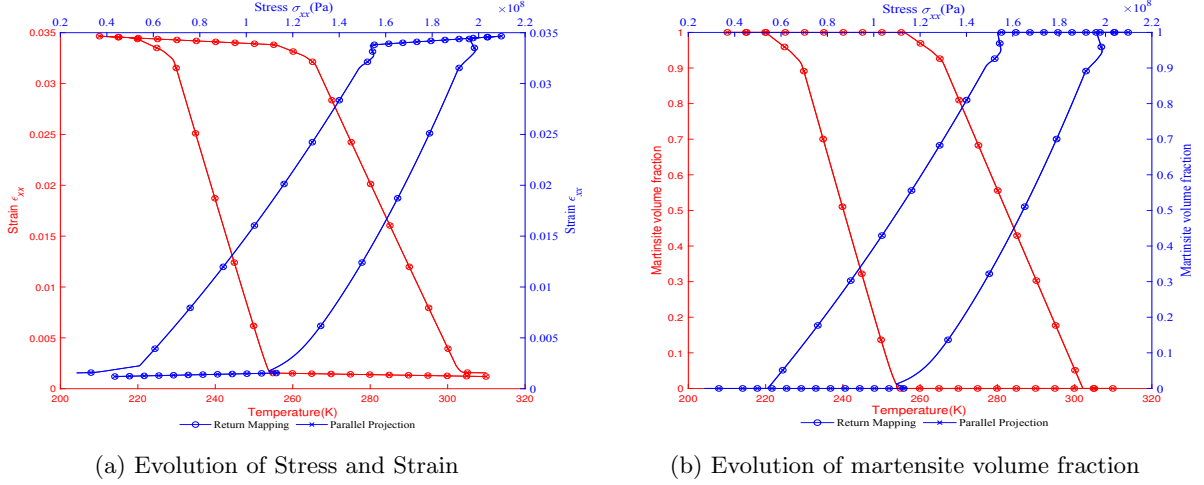


Figure 8: Simultaneous presence of TWSMEs and superelasticity in 3D bar under a temperature and loading cycle

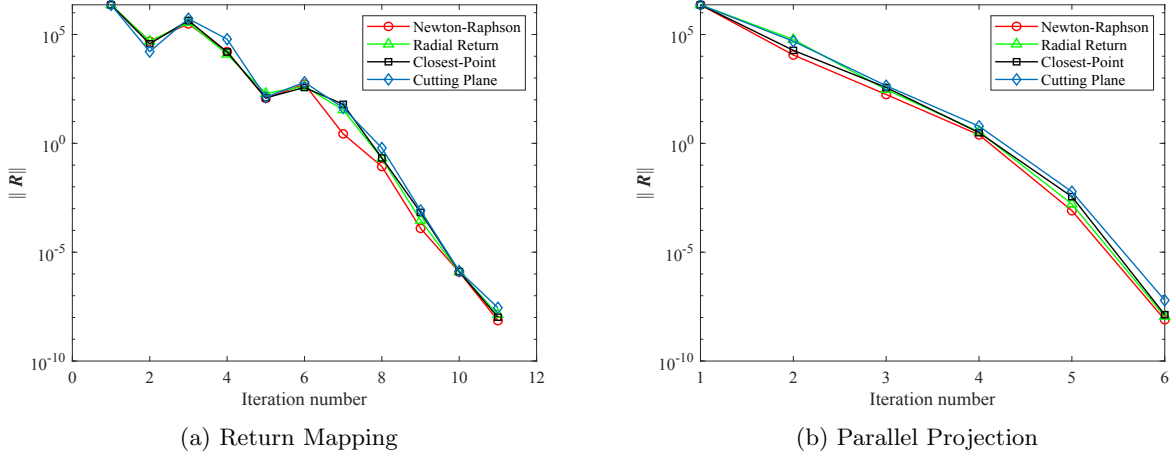


Figure 9: Convergence history of different schemes for updating internal state variables at  $T = 270\text{K}$

Tables 5 and 6 present the maximum thermomechanical loading increment allowed for the return mapping and parallel projection algorithms in simulating this 3D problem. We observe that parallel projection algorithm again exhibits larger increments than the return mapping algorithm, which is consistent to our findings in the 1D problem.

Methods	Newton-Raphson	Radial Return	Closest-Point	Cutting Plane
Return Mapping	1.04K	1.04K	1.04K	0.98K
Parallel Projection	4.7K	4.7K	4.7K	4.7K

Table 5: Approximate maximum temperature step, with fixed  $dF = 1 \times 10^5 \text{N/m}^2$

Table 7 shows the number of inner and outer iterations needed for a single-element at one time step, using the closest-point scheme with thermomechanical loading step size of  $dT = 0.1\text{K}$  and  $dF = 1 \times 10^5 \text{N/m}^2$ . Here,  $k$  is the global iteration counter and  $l$  is the local counter. Since the

Methods	Newton-Raphson	Radial Return	Closest-Point	Cutting Plane
Return Mapping	$1 \times 10^7 N$	$1 \times 10^7 N$	$1 \times 10^7 N$	$1 \times 10^7 N$
Parallel Projection	$5 \times 10^7 N$	$5 \times 10^7 N$	$5 \times 10^7 N$	$5 \times 10^7 N$

Table 6: Approximate maximum loading step, with fixed  $dT = 0.1K$

parallel projection uses a cross-iteration scheme, there is only a global counter  $k$ . As seen in the table, the parallel projection scheme requires 6 iterations, which is significantly less than the 11 *outer* iterations for the return mapping algorithm. In total the return mapping algorithm requires 11 outer iterations and 4 inner iteration for *each* of the 8 Gauss point for a total of  $N = 11 \cdot 4 \cdot 8 = 352$  computations versus  $N = 6 \cdot 8 = 48$  for the parallel projection method. Ultimately, the computed state variables for the two methods are identical (within the specified tolerances) as expected, since the same equations are solved.

Methods	$k$	$l/\text{Gauss Point}$	N	$\mathbf{d}_y^A$	$\xi_{G_A}$	$\epsilon_{yy}^{t G_A}$
Return Mapping	11	4	352	0.178241294	0.9711878	0.0320491973
Parallel Projection	6	/	48	0.178241294	0.9711880	0.0320491924

Table 7: Gauss point computation iteration count using the closet-point scheme,  $T = 230K$

Now, we test the problem with different mesh sizes and their corresponding computation time of the two algorithms, cf Figure 10. The parallel projection method yields a savings in computation time of greater than 50% without losing accuracy, implying its preference for modeling SMAs with large meshes and complicated boundary conditions.

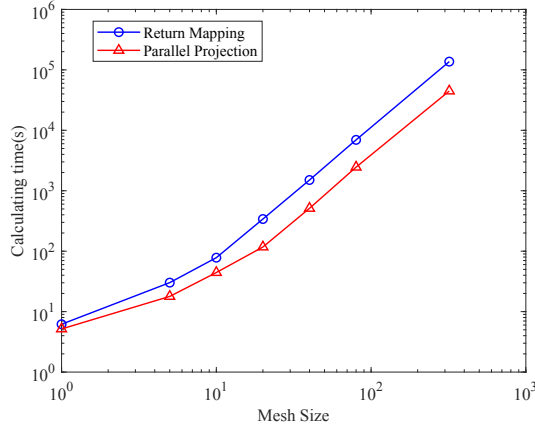


Figure 10: Comparison between Parallel Projection Algorithm and Return Mapping Algorithm

#### 4. Conclusions

We present a novel framework to improve upon the thermomechanical loading steps and computational efficiency of the classical return mapping algorithm in finite element analysis of SMAs. Instead of nested iteration, the proposed approach—the parallel projection algorithm—uses a sequential iterative scheme, which is able to significantly reduce computation time while not increasing the size of tangent matrix within the Newton-Raphson iterations. In addition, we use the Schur algorithm to provide the full Newton-Raphson updating scheme for the internal state variables. To test the robustness of the parallel projection algorithm, various numerical analysis examples

have been demonstrated. The simulation results for each case shows that parallel projection is able to achieve stable convergence, and the simulated thermomechanical responses are consistent with those obtained using established methods.

## Acknowledgements

This research was supported by the National Science Foundation through grant number CMMI1663566.

## Appendix

### A. Analytical Derivation of Newton-Raphson Updating Scheme

In this section, we present the derivation of the analytical solution of increment  $-\left(\frac{\partial \mathbf{H}_n}{\partial \boldsymbol{\nu}_n}\right)^{-1} \mathbf{H}_n$  for updating internal state variable vector  $\boldsymbol{\nu}$  through Newton-Raphson iteration methods. Due to the complexity of deriving the analytical solution of the aforementioned operator, previous research generally simplify the form of local residual  $\mathbf{H}$  to get degenerated derivations[14]. This might lead to a stability issue when using the results to update global state variable  $\mathbf{u}$ , since the tangent stiffness modulus  $\boldsymbol{\mathfrak{L}}$  gradually becomes more inaccurate as we simplify the residual. Another option is to numerically calculate the inverse of  $\frac{\partial \mathbf{H}_n}{\partial \boldsymbol{\nu}_n}$ . However, due to the large magnitude of compliance module  $S$  in the off-diagonal elements of the matrix, we always get ill-conditioned results.

Here, we use Schur algorithm to provide the analytical solution of inverse of  $\frac{\partial \mathbf{H}_n}{\partial \boldsymbol{\nu}_n}$  for the case of forward transformation ( $\dot{\xi} > 0$ ). In this way, we are able to solve the numerical issue of ill-conditioned inverse and unify the degenerated solution of previous research. For simplicity, we only present the derivation for the forward transformation in the paper. The derivation for inverse transformation can be obtained similarly following the derivation presented in the paper.

To start, we first represent the inverse of  $\partial \mathbf{H}_n / \partial \boldsymbol{\nu}_n$  using the Schur formulation [37].

$$\left(\frac{\partial \mathbf{H}_n}{\partial \boldsymbol{\nu}_n}\right)^{-1} = \begin{bmatrix} (\mathbb{A} + \mathbb{B}\mathbb{C})^{-1} & (\mathbb{A} + \mathbb{B}\mathbb{C})^{-1}\mathbb{B} \\ \mathbb{C}(\mathbb{A} + \mathbb{B}\mathbb{C})^{-1} & -\mathbf{I} + \mathbb{C}(\mathbb{A} + \mathbb{B}\mathbb{C})^{-1}\mathbb{B} \end{bmatrix} \quad (34)$$

with

$$\frac{\partial \mathbf{H}_n}{\partial \boldsymbol{\nu}_n} = \left[ \begin{array}{ccc|ccc} \partial_{\xi} \Phi_n & \mathbf{0}_{1 \times 6} & 0 & \partial_{\sigma_n} \Phi_n^T & & \\ \boldsymbol{\Lambda}_n & -\mathbf{I}_{6 \times 6} & \mathbf{0}_{6 \times 1} & \partial_{\sigma} \boldsymbol{\Lambda}_n : \Delta \xi_n & & \\ \Delta S & \mathbf{0}_{1 \times 6} & -\mathbf{I}_{1 \times 1} & \mathbf{0}_{1 \times 6} & & \\ \hline \mathbf{0}_{6 \times 1} & -\mathbf{S}_n^{-1} & -\mathbf{S}_n^{-1} : \boldsymbol{\sigma}_n & -\mathbf{I}_{6 \times 6} & & \end{array} \right] = \begin{bmatrix} \mathbb{A} & \mathbb{B} \\ \mathbb{C} & \mathbb{D} \end{bmatrix} \quad (35)$$

where  $\Delta \xi_n = \xi_n - \xi_{n-1}$  and  $\partial_{\sigma} \boldsymbol{\Lambda}$  only have nonzero value in forward transformation, following the definition of flow rule in Equation 11

Meanwhile, we define the local residual  $\mathbf{H}$  in block matrix form as

$$\mathbf{H}_n = \begin{Bmatrix} H_{\Phi} \\ H_{\varepsilon^t} \\ H_S \\ H_{\sigma} \end{Bmatrix} = \begin{Bmatrix} \widetilde{\mathbf{H}} \\ \mathbf{H}_{\sigma} \end{Bmatrix} \quad (36)$$

Then the increment of internal state variable vector for Newton-Raphson iteration can be expressed as below

$$\Delta \boldsymbol{\nu} = -\left(\frac{\partial \mathbf{H}_n}{\partial \boldsymbol{\nu}_n}\right)^{-1} \mathbf{H}_n = \begin{Bmatrix} -(\mathbb{A} + \mathbb{B}\mathbb{C})^{-1} \widetilde{\mathbf{H}} - (\mathbb{A} + \mathbb{B}\mathbb{C})^{-1} \mathbb{B} \mathbf{H}_{\sigma} \\ -\mathbb{C}(\mathbb{A} + \mathbb{B}\mathbb{C})^{-1} \widetilde{\mathbf{H}} - [-\mathbf{I} + \mathbb{C}(\mathbb{A} + \mathbb{B}\mathbb{C})^{-1} \mathbb{B}] \mathbf{H}_{\sigma} \end{Bmatrix} \quad (37)$$

Note that the solution of the shown in Equation 37 does not change the ill-conditioned characteristics of the matrix, since  $\mathbb{A}^{-1}$  is nearly singular due to the fact that the large number  $S$  is still off diagonal. Hence, the key to obtaining a non-singular solution of the operators lies in solving the inverse of  $(\mathbb{A} + \mathbb{B}\mathbb{C})$ . Here we use the Schur formulation again to calculate the inverse of the matrix.

$$\mathbb{A} + \mathbb{B}\mathbb{C} = \begin{bmatrix} (\mathbb{A}' + \mathbb{B}'\mathbb{C}')^{-1} & (\mathbb{A}' + \mathbb{B}'\mathbb{C}')^{-1}\mathbb{B}' \\ \mathbb{C}'(\mathbb{A}' + \mathbb{B}'\mathbb{C}')^{-1} & -\mathbf{I} + \mathbb{C}'(\mathbb{A}' + \mathbb{B}'\mathbb{C}')^{-1}\mathbb{B}' \end{bmatrix} \quad (38)$$

with

$$\mathbb{A} + \mathbb{B}\mathbb{C} = \left[ \begin{array}{c|cc} \frac{\partial_\xi \Phi_n}{\Lambda_n} & -\partial_\sigma \Phi_n : \mathbf{S}_n^{-1} & -\partial_\sigma \Phi_n : \mathbf{S}_n^{-1} : \sigma_n \\ \Delta S & -(\mathbf{S}_n + \partial_\sigma \Lambda_n : \Delta \xi_n) : \mathbf{S}_n^{-1} & -\partial_\sigma \Lambda_n : \Delta \xi_n : \mathbf{S}_n^{-1} : \sigma_n \\ \hline & \mathbf{0}_{1 \times 6} & -I_{1 \times 1} \end{array} \right] = \begin{bmatrix} \mathbb{A}' & \mathbb{B}' \\ \mathbb{C}' & \mathbb{D}' \end{bmatrix} \quad (39)$$

To solve  $(\mathbb{A} + \mathbb{B}\mathbb{C})^{-1}$ ,  $\mathbb{D}'^{-1}$  and  $(\mathbb{A}' - \mathbb{B}'\mathbb{D}'^{-1}\mathbb{C}')^{-1}$  need to be solved. Note that  $\partial_\sigma \Lambda$  belongs to the null space of  $\sigma$ , hence is not invertible [38]. However,  $(\mathbf{S}_n + \partial_\sigma \Lambda_n : \Delta \xi_n)$  is nonsingular. Defining  $\zeta_n = \mathbf{S}_n + \partial_\sigma \Lambda_n : \Delta \xi_n$ ,  $\mathbb{D}'^{-1}$  can be solved using Schur form as

$$\mathbb{D}'^{-1} = \begin{bmatrix} -\mathbf{S}_n : \zeta_n^{-1} & \mathbf{S}_n : \zeta_n^{-1} : \partial_\sigma \Lambda_n : \Delta \xi_n : \mathbf{S}_n^{-1} : \sigma_n \\ \mathbf{0}_{1 \times 6} & -I_{1 \times 1} \end{bmatrix} \quad (40)$$

With the above information, one can obtain that

$$\begin{aligned} \mathbb{B}'\mathbb{D}'^{-1} &= \left[ \partial_\sigma \Phi_n : \zeta_n^{-1} \quad \partial_\sigma \Phi_n : \zeta_n^{-1} : \mathbf{S}_n^{-1} : \mathbf{S}_n^{-1} : \sigma_n \right] \\ \mathbb{D}'^{-1}\mathbb{C}' &= \left[ -\mathbf{S}_n : \zeta_n^{-1} : (\Lambda_n - \partial_\sigma \Lambda_n : \Delta \xi_n : \mathbf{S}_n^{-1} : \sigma_n : \Delta S) \right. \\ &\quad \left. -\Delta S \right] = \begin{bmatrix} -\tilde{\Lambda}_n \\ -\Delta S \end{bmatrix} \end{aligned} \quad (41)$$

Then  $(\mathbb{A}' - \mathbb{B}'\mathbb{D}'^{-1}\mathbb{C}')^{-1} = -Q$  can be calculated as  $Q = \partial_\sigma \Phi_n : \zeta_n^{-1} : \partial_\sigma \Phi_n - \partial_\xi \Phi_n$  as a scalar. Hence the problem of singularity has been solved, and we have

$$\begin{aligned} \mathbb{C}(\mathbb{A} + \mathbb{B}\mathbb{C})^{-1} &= \left[ \frac{\zeta_n^{-1} : \partial_\sigma \Phi_n}{Q} \quad \mathfrak{L}_n \quad \mathfrak{L}_n : \mathbf{S}_n : \mathbf{S}_n^{-1} : \sigma_n \right] \\ \mathbb{C}(\mathbb{A} + \mathbb{B}\mathbb{C})^{-1}\mathbb{B} &= \frac{\zeta_n^{-1} : \partial_\sigma \Phi_n : \partial_\sigma \Phi_n^T}{Q} + \mathfrak{L}_n : \partial_\sigma \Lambda_n : \Delta \xi_n \end{aligned} \quad (42)$$

Ultimately, we can obtain the analytical solution of the increment of internal state variable for forward transformation as

$$\Delta \nu = \begin{Bmatrix} \delta \xi \\ \delta \varepsilon \\ \delta S \\ \delta \sigma \end{Bmatrix} = \begin{Bmatrix} \Delta \xi^* + \vartheta \\ \Delta \varepsilon^{t*} + \Lambda : \vartheta \\ \Delta S^* + H_S + \Delta S \cdot \vartheta \\ \Delta \sigma^* + \mathfrak{L}_n : \mathbf{S}_n : \Psi \end{Bmatrix} \quad (43)$$

where

$$\begin{aligned} \Delta \xi^* &= \frac{\Phi_n - \partial_\sigma \Phi_n : \zeta_n^{-1} : H_{\varepsilon^t}}{\partial_\sigma \Phi_n : \zeta_n^{-1} : \partial_\sigma \Phi_n - \partial_\xi \Phi_n} & (\dot{\xi} > 0) \\ \Delta \sigma^* &= \zeta_n^{-1} : [-H_{\varepsilon^t} - \Delta \xi^* : \partial_\sigma \Phi_n] & (\dot{\xi} > 0) \\ \Delta \varepsilon^{t*} &= -\mathbf{S}_n : \Delta \sigma^* - [\Delta S : \sigma_n + \Delta \alpha(T_n - T_0)] \Delta \xi^* \\ \Delta S^* &= \Delta S \Delta \xi^* \\ \Psi &= \mathbf{H}_\sigma - \mathbf{S}_n^{-1} : \sigma_n : H_S \\ \vartheta &= \frac{\partial_\sigma \Phi_n}{\partial_\sigma \Phi_n : \zeta_n^{-1} : \partial_\sigma \Phi_n^{(k)} - \partial_\xi \Phi_n} : \zeta_n^{-1} : \mathbf{S}_n : \Psi & (\dot{\xi} > 0) \end{aligned} \quad (44)$$

For inverse transformation,  $\zeta_n = \mathbf{S}_n$  since  $\partial_\sigma \Lambda_n = 0$ . According to the definition of  $\Phi$  in Equation ??, we shall only have changes in  $\Delta\xi^*$ ,  $\Delta\sigma^*$  and  $\vartheta$ , as

$$\begin{aligned}\Delta\xi^* &= \frac{\Phi_n - \partial_\sigma \Phi_n : \mathbf{S}_n^{-1} : H_{\varepsilon t}}{-\partial_\sigma \Phi_n : \mathbf{S}_n^{-1} : \partial_\sigma \Phi_n - \partial_\xi \Phi_n} \quad (\dot{\xi} < 0) \\ \Delta\sigma^* &= \mathbf{S}_n^{-1} : [-H_{\varepsilon t} + \Delta\xi^* : \partial_\sigma \Phi_n] \quad (\dot{\xi} < 0) \\ \vartheta &= \frac{\partial_\sigma \Phi_n}{-\partial_\sigma \Phi_n : \mathbf{S}_n^{-1} : \partial_\sigma \Phi_n^{(k)} - \partial_\xi \Phi_n} : \Psi \quad (\dot{\xi} < 0)\end{aligned}\quad (45)$$

Then, the consistent tangent operator  $(\partial \mathbf{R} / \partial \boldsymbol{\nu})(d\mathbf{u} / d\boldsymbol{\nu})$  can be derived with the aforementioned analytical solution of  $(\partial \mathbf{H} / \partial \boldsymbol{\nu})^{-1}$ . Known that

$$\begin{aligned}\frac{\partial \mathbf{R}_{\text{el},n}}{\partial \boldsymbol{\nu}_n} &= [0 \quad 0 \quad 0 \quad w \mathbf{B}^T \det \mathbf{J}] \\ \frac{\partial \mathbf{H}_{\text{G},n}}{\partial \mathbf{u}_{\text{el},n}} &= \begin{bmatrix} 0 \\ 0 \\ 0 \\ \mathbf{S}_n^{-1} : \mathbf{B} \end{bmatrix}\end{aligned}\quad (46)$$

and  $d\boldsymbol{\nu} / d\mathbf{u} = -(\partial \mathbf{H} / \partial \boldsymbol{\nu})^{-1}(\partial \mathbf{H} / \partial \mathbf{u})$  from Equation 23, the consistent tangent operator can be derived as

$$\begin{aligned}\frac{\partial \mathbf{R}_n}{\partial \boldsymbol{\nu}_n} \frac{d\boldsymbol{\nu}}{d\mathbf{u}} &= - \bigwedge_{\text{el}} \sum_{\text{G}} \frac{\partial \mathbf{R}_n}{\partial \boldsymbol{\nu}_{\text{G},n}} \left( \frac{\partial \mathbf{H}_n}{\partial \boldsymbol{\nu}_{\text{G},n}} \right)^{-1} \frac{\partial \mathbf{H}_{\text{G},n}}{\partial \mathbf{u}_{\text{el},n}} \\ &= \bigwedge_{\text{el}} \sum_{\text{G}} w \mathbf{B}_{\text{G}}^T [\mathbf{I} - \mathbb{C}(\mathbb{A} + \mathbb{B}\mathbb{C})^{-1} \mathbb{B}]_{\text{G}} : \mathbf{S}_{\text{G},n}^{-1} \mathbf{B}_{\text{G}} \det \mathbf{J}_{\text{G}} \\ &= \bigwedge_{\text{el}} \sum_{\text{G}} w \mathbf{B}_{\text{G}}^T \boldsymbol{\mathfrak{L}}_n \mathbf{B}_{\text{G}} \det \mathbf{J}_{\text{G}}\end{aligned}\quad (47)$$

where

$$\boldsymbol{\mathfrak{L}}_n = \begin{cases} \zeta_n^{-1} - \frac{\zeta_n^{-1} : \partial_\sigma \Phi_n \otimes \zeta_n^{-1} : \partial_\sigma \Phi_n}{\partial_\sigma \Phi_n : \zeta_n^{-1} : \partial_\sigma \Phi_n - \partial_\xi \Phi} & \dot{\xi} > 0 \\ \mathbf{S}_n^{-1} - \frac{\mathbf{S}_n^{-1} : \partial_\sigma \Phi_n \otimes \mathbf{S}_n^{-1} : \partial_\sigma \Phi_n}{\partial_\sigma \Phi_n : \mathbf{S}_n^{-1} : \partial_\sigma \Phi_n + \partial_\xi \Phi} & \dot{\xi} < 0 \end{cases}\quad (48)$$

In addition,  $(\partial \mathbf{H} / \partial \boldsymbol{\nu})^{-1}(\partial \mathbf{H} / \partial \mathbf{u})$  can be expressed as

$$\left( \frac{\partial \mathbf{H}_n}{\partial \boldsymbol{\nu}_n} \right)^{-1} \frac{\partial \mathbf{H}_n}{\partial \mathbf{u}_n} = \begin{cases} \left[ \begin{array}{c} -\frac{\partial_\sigma \Phi_n^T : \zeta_n^{-1}}{\partial_\sigma \Phi_n : \zeta_n^{-1} : \partial_\sigma \Phi_n - \partial_\xi \Phi} \\ -\frac{\tilde{\Lambda}_n : \partial_\sigma \Phi_n^T}{\partial_\sigma \Phi_n : \zeta_n^{-1} : \partial_\sigma \Phi_n - \partial_\xi \Phi} : \zeta_n^{-1} + \mathbf{S}_n : \zeta_n^{-1} - \mathbf{I}_{6 \times 6} \\ -\frac{\Delta S : \partial_\sigma \Phi_n^T}{\partial_\sigma \Phi_n : \zeta_n^{-1} : \partial_\sigma \Phi_n - \partial_\xi \Phi} : \zeta_n^{-1} \\ -\boldsymbol{\mathfrak{L}}_n \end{array} \right] \mathbf{B} & \dot{\xi} > 0 \\ \left[ \begin{array}{c} -\frac{\partial_\sigma \Phi_n^T : \mathbf{S}_n^{-1}}{\partial_\sigma \Phi_n : \mathbf{S}_n^{-1} : \partial_\sigma \Phi_n + \partial_\xi \Phi} \\ \left[ \begin{array}{c} \Lambda_n \\ \Delta S \end{array} \right] : \partial_\sigma \Phi_n^T : \mathbf{S}_n^{-1} \\ -\boldsymbol{\mathfrak{L}}_n \end{array} \right] \mathbf{B} & \dot{\xi} < 0 \end{cases}\quad (49)$$

where

$$\tilde{\Lambda}_n = \mathbf{S}_n : \zeta_n^{-1} : (\Lambda_n - \partial_\sigma \Lambda_n : \Delta \zeta_n : \mathbf{S}_n^{-1} : \mathbf{I}_{6 \times 6} : \boldsymbol{\sigma}_n : \Delta S)\quad (50)$$

and  $(\partial \mathbf{R} / \partial \boldsymbol{\nu})(\partial \mathbf{H} / \partial \boldsymbol{\nu})^{-1}$  can be obtained as

$$\frac{\partial \mathbf{R}_n}{\partial \boldsymbol{\nu}_n} \left( \frac{\partial \mathbf{H}_n}{\partial \boldsymbol{\nu}_n} \right)^{-1} = \begin{cases} w \mathbf{B}^T \begin{bmatrix} \frac{\zeta_n^{-1} : \partial_\sigma \Phi_n}{Q} & \boldsymbol{\mathcal{L}}_n & \boldsymbol{\mathcal{L}}_n : \boldsymbol{\mathcal{C}}^{-1} : \boldsymbol{\sigma}_n & -\boldsymbol{\mathcal{L}}_n : \mathbf{S}_n \end{bmatrix} \det \mathbf{J} & \dot{\xi} > 0 \\ w \mathbf{B}^T \begin{bmatrix} \frac{\mathbf{S}_n^{-1} : \partial_\sigma \Phi_n}{Q} & \boldsymbol{\mathcal{L}}_n & \boldsymbol{\mathcal{L}}_n : \boldsymbol{\mathcal{C}}^{-1} : \boldsymbol{\sigma}_n & -\boldsymbol{\mathcal{L}}_n : \mathbf{S}_n \end{bmatrix} \det \mathbf{J} & \dot{\xi} < 0 \end{cases} \quad (51)$$

## References

- [1] T. W. Duerig, K. Melton, and D. Stöckel, *Engineering aspects of shape memory alloys*. Butterworth-heinemann, 2013.
- [2] K. Otsuka and C. M. Wayman, *Shape memory materials*. Cambridge university press, 1999.
- [3] Q. P. Sun and K. C. Hwang, “Micromechanics modelling for the constitutive behavior of polycrystalline shape memory alloys—i. derivation of general relations,” *Journal of the Mechanics and Physics of Solids*, vol. 41, no. 1, pp. 1–17, 1993.
- [4] Q. P. Sun and K. C. Hwang, “Micromechanics modelling for the constitutive behavior of polycrystalline shape memory alloys—ii. study of the individual phenomena,” *Journal of the Mechanics and Physics of Solids*, vol. 41, no. 1, pp. 19–33, 1993.
- [5] K. Bhattacharya and R. V. Kohn, “Symmetry, texture and the recoverable strain of shape-memory polycrystals,” *Acta materialia*, vol. 44, no. 2, pp. 529–542, 1996.
- [6] K. Bhattacharya *et al.*, *Microstructure of martensite: why it forms and how it gives rise to the shape-memory effect*, vol. 2. Oxford University Press, 2003.
- [7] C. Cisse, W. Zaki, and T. B. Zineb, “A review of constitutive models and modeling techniques for shape memory alloys,” *International Journal of Plasticity*, vol. 76, pp. 244–284, 2016.
- [8] M. Frost, B. Benešová, and P. Sedlák, “A microscopically motivated constitutive model for shape memory alloys: formulation, analysis and computations,” *Mathematics and Mechanics of Solids*, vol. 21, no. 3, pp. 358–382, 2016.
- [9] K. Tanaka, F. Nishimura, T. Hayashi, H. Tobushi, and C. Lexcellent, “Phenomenological analysis on subloops and cyclic behavior in shape memory alloys under mechanical and/or thermal loads,” *Mechanics of Materials*, vol. 19, no. 4, pp. 281–292, 1995.
- [10] C. Liang and C. Rogers, “A multi-dimensional constitutive model for shape memory alloys,” *Journal of Engineering Mathematics*, vol. 26, no. 3, pp. 429–443, 1992.
- [11] C. Liang and C. A. Rogers, “One-dimensional thermomechanical constitutive relations for shape memory materials,” *Journal of intelligent material systems and structures*, vol. 8, no. 4, pp. 285–302, 1997.
- [12] J. G. Boyd and D. C. Lagoudas, “A thermodynamical constitutive model for shape memory materials. part i. the monolithic shape memory alloy,” *International Journal of Plasticity*, vol. 12, no. 6, pp. 805–842, 1996.
- [13] J. G. Boyd and D. C. Lagoudas, “A thermodynamical constitutive model for shape memory materials. part ii. the sma composite material,” *International Journal of Plasticity*, vol. 12, no. 7, pp. 843–873, 1996.

- [14] D. C. Lagoudas, *Shape memory alloys: modeling and engineering applications*. Springer, 2008.
- [15] D. Lagoudas, D. Hartl, Y. Chemisky, L. Machado, and P. Popov, “Constitutive model for the numerical analysis of phase transformation in polycrystalline shape memory alloys,” *International Journal of Plasticity*, vol. 32, pp. 155–183, 2012.
- [16] C. Yu, G. Kang, Q. Kan, and D. Song, “A micromechanical constitutive model based on crystal plasticity for thermo-mechanical cyclic deformation of niti shape memory alloys,” *International Journal of Plasticity*, vol. 44, pp. 161–191, 2013.
- [17] C. Yu, G. Kang, and Q. Kan, “Crystal plasticity based constitutive model of niti shape memory alloy considering different mechanisms of inelastic deformation,” *International Journal of Plasticity*, vol. 54, pp. 132–162, 2014.
- [18] C. LExcellent and J. Rejzner, “Modeling of the strain rate effect, creep and relaxation of a ni-ti shape memory alloy under tension (compression)-torsional proportional loading in the pseudoelastic range,” *Smart materials and structures*, vol. 9, no. 5, p. 613, 2000.
- [19] D. C. Lagoudas, G. Chatzigeorgiou, and P. K. Kumar, “Modeling and experimental study of simultaneous creep and transformation in polycrystalline high-temperature shape memory alloys,” *Journal of Intelligent Material Systems and Structures*, vol. 20, no. 18, pp. 2257–2267, 2009.
- [20] D. J. Hartl, G. Chatzigeorgiou, and D. C. Lagoudas, “Three-dimensional modeling and numerical analysis of rate-dependent irrecoverable deformation in shape memory alloys,” *International Journal of Plasticity*, vol. 26, no. 10, pp. 1485–1507, 2010.
- [21] A. Paiva, M. A. Savi, A. M. B. Braga, and P. M. C. L. Pacheco, “A constitutive model for shape memory alloys considering tensile–compressive asymmetry and plasticity,” *International Journal of Solids and Structures*, vol. 42, no. 11-12, pp. 3439–3457, 2005.
- [22] R. Mehrabi, M. Kadkhodaei, and M. Elahinia, “Constitutive modeling of tension-torsion coupling and tension-compression asymmetry in niti shape memory alloys,” *Smart materials and structures*, vol. 23, no. 7, p. 075021, 2014.
- [23] L. Xu, T. Baxevanis, and D. Lagoudas, “A three-dimensional constitutive model for the martensitic transformation in polycrystalline shape memory alloys under large deformation,” *Smart Materials and Structures*, vol. 28, no. 7, p. 074004, 2019.
- [24] L. C. Brinson, “One-dimensional constitutive behavior of shape memory alloys: thermomechanical derivation with non-constant material functions and redefined martensite internal variable,” *Journal of intelligent material systems and structures*, vol. 4, no. 2, pp. 229–242, 1993.
- [25] S. Leclercq and C. LExcellent, “A general macroscopic description of the thermomechanical behavior of shape memory alloys,” *Journal of the Mechanics and Physics of Solids*, vol. 44, no. 6, pp. 953–980, 1996.
- [26] S. Reese and D. Christ, “Finite deformation pseudo-elasticity of shape memory alloys—constitutive modelling and finite element implementation,” *International Journal of Plasticity*, vol. 24, no. 3, pp. 455–482, 2008.



- [27] J. Arghavani, F. Auricchio, R. Naghdabadi, A. Reali, and S. Sohrabpour, “A 3-d phenomenological constitutive model for shape memory alloys under multiaxial loadings,” *International Journal of Plasticity*, vol. 26, no. 7, pp. 976–991, 2010.
- [28] J. Wang, Z. Moumni, W. Zhang, Y. Xu, and W. Zaki, “A 3d finite-strain-based constitutive model for shape memory alloys accounting for thermomechanical coupling and martensite reorientation,” *Smart Materials and Structures*, vol. 26, no. 6, p. 065006, 2017.
- [29] L. Brinson and R. Lammering, “Finite element analysis of the behavior of shape memory alloys and their applications,” *International Journal of solids and structures*, vol. 30, no. 23, pp. 3261–3280, 1993.
- [30] M. Qidwai and D. Lagoudas, “Numerical implementation of a shape memory alloy thermo-mechanical constitutive model using return mapping algorithms,” *International Journal for Numerical Methods in Engineering*, vol. 47, no. 6, pp. 1123–1168, 2000.
- [31] J. C. Simo and T. J. Hughes, *Computational inelasticity*, vol. 7. Springer Science & Business Media, 2006.
- [32] D. V. Kulkarni, D. A. Tortorelli, and M. Wallin, “A newton–schur alternative to the consistent tangent approach in computational plasticity,” *Computer methods in applied mechanics and engineering*, vol. 196, no. 7, pp. 1169–1177, 2007.
- [33] D. C. Lagoudas, Z. Bo, and M. A. Qidwai, “A unified thermodynamic constitutive model for sma and finite element analysis of active metal matrix composites,” *Mechanics of composite materials and structures*, vol. 3, no. 2, pp. 153–179, 1996.
- [34] C. Kittel and H. Kroemer, “Thermal physics,” 1998.
- [35] M. Qidwai and D. Lagoudas, “On thermomechanics and transformation surfaces of polycrystalline niti shape memory alloy material,” *International journal of plasticity*, vol. 16, no. 10-11, pp. 1309–1343, 2000.
- [36] M. Ortiz and J. B. Martin, “Symmetry-preserving return mapping algorithms and incrementally extremal paths: a unification of concepts,” *International Journal for Numerical Methods in Engineering*, vol. 28, no. 8, pp. 1839–1853, 1989.
- [37] F. Zhang, *The Schur complement and its applications*, vol. 4. Springer Science & Business Media, 2006.
- [38] A. S. Householder, *Principles of numerical analysis*. Courier Corporation, 2006.